Superconductivity of VSe_2 under pressure and charge doping: Suppressed charge density wave

Xin-Peng Fu,[1,2,3] Zhen-Guo Fu,[1,2,*] Chong-Jie Mo,[4] Bao-Tian Wang,[5] Peng-Fei Liu,[5] Guo-Jun Zhao,[6] Ning Hao,[7] and Ping Zhang[1,2,8,†]

[1]*Institute of Applied Physics and Computational Mathematics, Beijing 100088, China*
[2]*National Key Laboratory of Computational Physics, Beijing 100088, China*
[3]*Graduate School, China Academy of Engineering Physics, Beijing 100088, China*
[4]*Beijing Computational Science Research Center, Beijing 100193, China*
[5]*Spallation Neutron Source Science Center, Dongguan 523803, China*
[6]*School of Physical Science and Technology, Inner Mongolia University, Hohhot 010021, China*
[7]*Anhui Province Key Laboratory of Low-Energy Quantum Materials and Devices, High Magnetic Field Laboratory, HFIPS, Chinese Academy of Sciences, Hefei, Anhui 230031, China*
[8]*School of Physics and Physical Engineering, Qufu Normal University, Qufu 273165, China*

(Received 16 January 2024; revised 1 June 2024; accepted 17 June 2024; published 1 July 2024)

By employing the first-principles calculations, the influence mechanism of external pressure and charge doping on the electron-phonon coupling (EPC) and superconductivity (SC) of bulk VSe_2 is investigated. Our calculations reveal that with increasing pressure the charge density wave (CDW) of 1T-VSe_2 is gradually suppressed, and a SC state subsequently emerges which is accompanied by a structural phase transition from the trigonal phase to a monoclinic phase at 15.5 GPa. Increasing pressure from 15.5 to 35 GPa, the SC transition temperature T_c of VSe_2 slightly increases from 4.2 to 5.2 K and no SC dome is found, which are in good agreement with the previous experimental results [S. Sahoo *et al.*, Phys. Rev. B **101**, 014514 (2020)]. Through electron- or hole-doping (denoted by n_e and n_h), the CDW order of the trigonal phase can be suppressed and SC states with T_c greater than 10.5 and 9.0 K, respectively, emerge. The highest T_c under charge doping can be up to about 12 K, and a weak double-dome like dependence of T_c on n_e and n_h is found. Combining systematical analysis of effects of pressure and charge doping, we demonstrate that the Kohn anomalies of phonons at certain Q points associated with the in-plane vibrations of V atoms play key roles in strengthening the EPC, which brings about the intriguing SC in VSe_2. However, due to the weak pressure-induced modifications of phonon spectrum as well as Fermi surface (FS), the changes of EPC and T_c caused by pressure are not significant. Interestingly, charge doping will produce a local flat band along ΓA direction near the FS, which is mainly contributed by V 3d-orbitals, and result in large values of electronic density of states at Fermi level. Therefore, the effects caused by charge doping to the electronic structures, phonon anomalies, EPC, and T_c are evident. Our findings may provide a promising understanding to the pressure and doping-dependent SC of VSe_2, and may be valuable for designing new materials with enhanced SC through the strategic manipulation of electronic and phononic properties.

DOI: 10.1103/PhysRevB.110.014501

I. INTRODUCTION

With the advanced development of material preparation technology in recent years, a variety of two-dimensional (2D) materials, such as graphene [1], FeSe monolayer superconductors [2–4], 2D MXenes [5], and transition metal dichalcogenides (TMDCs) [6–9], have been successfully obtained. Among them, due to the rich physical properties, such as Mott insulator state, topological insulator state, Weyl semimetal state, magnetism state, charge density wave (CDW) state, superconductivity (SC) state, and so on embedded in, TMDCs have attracted great interest in the modern condensed matter physics field. The remarkable electronic interactions and electron-phonon coupling (EPC) in TMDCs make them potential candidates for studying the balance and transition between these electronic states.

Recently, extensive endeavors have been devoted to exploring novel unconventional superconductors in WTe_2 and $MoTe_2$ via the applications of pressure and (electrostatic) charge doping in experiments [10–18] since they can unveil the relationship between SC phase and topological insulator phase as well as Weyl semimetal phase in the layered TMDCs and provide important insights about the superconducting mechanism. In addition to the topological properties, due to the effects of dramatic EPC and FS instability, the emergence of SC state accompanied the suppression of CDW state in various layered TMDCs materials (e.g., TaS_2 [19–28], $TiSe_2$ [29–33], $TaSe_2$ [23,34–37], $MoTe_2$ [17,38–42], $NbSe_2$ [43–59], MoS_2 [60,61], VSe_2 [62,63], and others [64–72]) has been frequently observed, which reveals the complex competition and coexistence behaviors between SC state and CDW state in response to external manipulations such as high pressure, chemical doping, electric field, and thickness.

*Contact author: fu_zhenguo@iapcm.ac.cn
†Contact author: zhang_ping@iapcm.ac.cn

It is interesting and important that the same external parameters may cause completely different impact patterns in different TMDCs. For example, the superconducting transition temperature T_c of $NbSe_2$ exhibits a positive correlation with the thickness of sample, which has been explained by the weaker Coulomb screening, the weakening of interlayer Cooper pairs, and the reduction of superfluid stiffness [51]. In strictly contrast to the case of $NbSe_2$, the T_c of TaS_2 performs a negative connection with the thickness, which is attributed to a suppression of the effective EPC constant with increasing the number of layers [22]. Moreover, by applying external pressure to 1T-TaS_2, the transition from Mott state to a textured CDW state, and then into a SC state coexisting with CDW in a proper pressure regime has been observed [20]. However, through controllable high pressure [30], or external electric field effect [31], the CDW and SC in 1T-$TiSe_2$ compete with each other suggesting that spatially modulated electronic states are fundamental to the appearance of 2D SC with different superconducting domes.

Remarkably differing from many TMDCs, recent investigations have revealed some interesting findings about VSe_2, specifically in the contexts of its CDW and SC properties. On the one hand, theoretical predictions have suggested that because of the strong EPC, a $\sqrt{7} \times \sqrt{3}$ 2D CDW superstructures may be favored in the freestanding monolayer 1T-VSe_2 [73]. While depending on the substrate-induced strain as well as the preparation conditions [74–79], various CDW phases, including 2×2, 4×4, $2 \times \sqrt{3}$, $4 \times \sqrt{3}$, and $\sqrt{7} \times \sqrt{3}$ 2D CDW superstructures have been observed experimentally in the monolayer 1T-VSe_2 [80–87]. On the other hand, because of the strong FS nesting and EPC effects, a $4 \times 4 \times 3$ 3D CDW superstructure is favored in the bulk 1T-VSe_2 [73,88–94]. Furthermore, under extremely high pressure conditions exceeding 15 GPa, VSe_2 exhibited a SC state with $T_c \sim 4$ K accompanied by the suppression of CDW and a structural phase transition from the original 2D van der Waals (vdW) layered structure into a 3D superstructure with monoclinic symmetry [62,63,95]. In addition, Sahoo and his collaborators have found that the dependence of T_c on the external pressure is negligible [62], which differs from the increase or the dome-shaped behavior observed in many other TMDCs. These experimental findings about the CDW and SC phases in the monolayer and bulk 1T-VSe_2 may have significant implications for advancing our understanding of the relationship among dimensionality, structure, CDW, and SC phenomena in TMDCs.

Instead of either reducing the sample thickness or applying high pressure, ion intercalation, which can strongly affect the interlayer interaction and carrier concentration in the layered materials, is another quite generic technique for controlling and modulating the SC and CDW states, and has been readily extended to a large group of TMDCs materials (for example, TaS_2 [19], $TiSe_2$ [29], $TaSe_2$ [35], $MoTe_2$ and WTe_2 [39,41,42], $NbSe_2$ [44,45,48,52,55,57,58], $SnSe_2$ [66], and so on) with a wide variety of cations. It is clear to us that tuning the physical properties of CDW and SC states by applying pressure, reducing thickness, as well as chemical (or charge) doping are common tools in the condensed matter field. Nevertheless, to our best knowledge, there was no theoretical work about the pressure and charge doping induced interplay of SC and CDW in 1T-VSe_2 to date, and the origin of experimentally observed no-dome-type evolution of T_c with pressure seems remain puzzled. Owing to the importance from the perspectives of both enriching the fundamental physics and intriguing properties of layered materials, it is timely to provide a theoretical analysis of the pressure and charge doping-dependent SC in the bulk VSe_2.

Therefore, in this work, we systematically study the effect mechanism of external pressure and charge doping on the EPC and SC properties in VSe_2 by following the first-principles calculations. Our calculations show that strong external pressure and proper charge doping can significantly eliminate the imaginary frequency of the hexagonal VSe_2, so that the CDW phase is effectively suppressed, and the SC state is successfully induced. Especially, a structural phase transition by high pressure determined by Sereika *et al.* in Ref. [63] is considered. While the influence of electron doping (e-doping) and hole doping (h-doping) on the structure and lattice constants of bulk 1T-VSe_2 is ignored in all calculations. On one side, in the presence of high pressure greater than 15 GPa, the values and no-dome like evolution of our calculated T_c are well consistent with the experimental measurements [62]. On the other side, in the presence of proper e- and h-doping, we find a weak double-dome like dependence of T_c on the concentration of doped electrons and holes, which is not observed in any TMDCs materials so far. Furthermore, it is worth notice that the value of T_c is significantly enhanced up to 9 to 12 K by charge doping in 1T-VSe_2, which is two to three times the T_c caused by pressure, and also higher than that of other (ion intercalated) TMDCs materials, such as 2H-$NbSe_2$ intercalated by Li, Rb, Sn, Cu, Fe, Ca, and others, reported in previous literatures. By analyzing the effects of pressure and charge doping, we found that in VSe_2, Kohn anomalies of phonons at specific Q-points associated with the in-plane vibration of V atoms play a vital role in the EPC that leads to SC. However, pressure has a weak impact on the phonon spectrum and FS stability, resulting in insignificant changes to EPC and T_c. However, charge doping produces a local flat band near the FS along the ΓA direction, which is caused by V's d-orbital. This flat band leads to a divergent density of states, causing T_c to be much higher than in dispersive bands. This may be the crucial physical mechanism that the charge doping-dependent T_c is more than twice as high as the pressure-dependent T_c in VSe_2. These findings shade light on the understanding of the mechanism of SC and the suppression of CDW in bulk VSe_2 induced by pressure and charge doping, and demonstrate furthermore the great potential of pressure and charge doping for engineering electronic properties of vdW layered TMDCs.

This paper is organized as follows. In Sec. II, the computational methods are summarized. In Sec. III, the pressure-dependent SC in the 3D superstructure of VSe_2 with monoclinic symmetry are discussed. In Sec. IV, we analyze the charge doping-dependent SC in the bulk 1T-VSe_2. Finally, Sec. V gives the conclusions of this work.

II. COMPUTATIONAL METHODS

The calculations about electronic structures are performed using the density functional theory (DFT) as implemented in the QUANTUM ESPRESSO code [96,97]. The

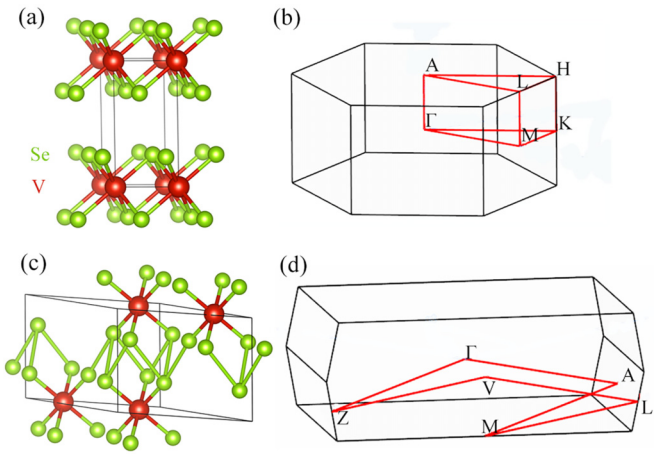

FIG. 1. (a) The crystal structure of 1T-VSe_2 with trigonal symmetry in the absence of pressure, and (b) the corresponding BZ. (c) The scheme of crystal structure of VSe_2 with monoclinic phase induced by a high pressure, and (d) the corresponding BZ. The red and green ball represent V and Se atoms, respectively.

interactions between electrons and ion cores are described by the projected augmented wave (PAW) potentials [98] with the $3s^2 3p^6 3d^3 4s^2$ and $4s^2 4p^4$ configurations treated as valence electrons for V and Se, respectively. The generalized gradient approximation (GGA) functional of Perdew-Burke-Ernzerhof (PBE) is adopted to treat the exchange-correlation interaction [99]. Furthermore, the phonon dispersion curves and EPC are calculated within the framework of density functional perturbation theory (DFPT) [100]. The FSs colored as a function of an arbitrary scalar quantities are drawn by employing the FERMISURFER program [101]. In addition, the EPC constant λ and the superconducting transition temperature T_c are calculated based on the Migdal-Eliashberg theory [102,103]. The detailed descriptions on the computational methods are presented in Appendix A.

III. PRESSURE-DEPENDENT SUPERCONDUCTIVITY IN 1T′-VSe_2

A. Atomic structures

The undistorted 1T-VSe_2 belongs to the space group of $P\bar{3}m1$ (No. 164) with trigonal symmetry, as shown in Figs. 1(a) and 1(b). The up and down Se atoms within each trilayer have the same horizontal coordinates. The optimized lattice constants of 1T-VSe_2 are $a = 3.326$ Å and $c = 6.187$ Å, in good agreement with the experimental values of 3.35 Å and 6.11 Å [105]. Bulk 1T-VSe_2 displayes a CDW transition at 110 K, exhibiting a $4 \times 4 \times 3$ CDW superstructure with a CDW wave vector $\boldsymbol{Q}_{\mathrm{CDW}} = 0.25a^* + 0.3c^*$ [90,91]. However, the CDW phase will be sufficiently suppressed by applying external pressure or doping charges into the system.

On one side, when the applied pressure is greater than 15.5 GPa, the vdW bonding in bulk 1T-VSe_2 is transformed to the Heisenberg covalent bonding between layers, and then an isostructural transition occurs, which results in a novel superstructure with monoclinic symmetry belonging to the space group $C2/m$ (No. 12), seeing Figs. 1(d) and 1(e). Our calculated lattice constants for this high-pressure ($P \geqslant 15.5$ GPa) phase of VSe_2 are also well consistent with the previous results [63]. For instance, for the case of $P = 35$ GPa, the optimized lattice constants are $a = 15.983$ Å, $b = 3.074$ Å, $c = 5.257$ Å, and $\beta = 89.94^\circ$ in good agreement with the reports in Ref. [63]. For convenience of expression and distinction from the original structure of 1T-VSe_2, in the following discussions, the high-pressure monoclinic structure is denoted as 1T′-VSe_2.

On the other side, it has been pointed out in other layer materials that when the concentration of charge doping is several 10^{21} cm^{-3}, the modification of lattice constant is negligible [106–108]. In the present work, we also checked the effect of charge doping on the structure of 1T-VSe_2. We find that the lattice change caused by doping is less than 2% within the range of charge doping concentration considered herein. Therefore, the structure differences after charge doping is ignored in all of the following calculations.

B. Electronic structures

As mentioned above, under a high pressure greater than 15.5 GPa, the bulk VSe_2 undergoes structural phase transition and forms a superstructure of 1T′-VSe_2. Correspondingly, the symmetry of the system is reduced, that is, the symmetry is lowered from triangular symmetry (D_{3h}) to monoclinic symmetry (C_{2h}). Simultaneously, the CDW phase is completely suppressed and the system exhibits attractive superconducting properties. To explore the physical mechanism of pressure-dependent SC, we first analyze the electronic structures of 1T′-VSe_2.

Our calculated orbital-resolved band structures, the corresponding partial electronic DOSs and three-dimensional FSs of 1T′ -VSe_2 are presented in Fig. 2, in which the left panels 2(a)–2(e), middle panels 2(a)–2(e), and right panels 2(a)–2(e) are for $P = 16$, 22, and 35 GPa, respectively. It is clear from Fig. 2 that the band structures show metallic features with valence band (VB) and conduction band (CB) crossing the Fermi level. The V-d orbitals are dominant components for conduction and valence bands, seeing Figs. 2(a), 2(f), and 2(k). Furthermore, Figs. 2(b), 2(g), and 2(l) indicate that the contributions from Se-p orbitals are small but visible around the high-symmetric points L, M, Γ and Z. In addition, those from Se-s orbital are negligible as shown in Figs. 2(c), 2(h), and 2(m).

To provide a microscopic understanding of the electronic structures of VSe_2 under high pressure, we calculate the hopping parameters of the states near the Fermi level by calculating the maximally localized Wannier functions (MLWFs) using the Wannier90 code [109]. The initial projections are chosen to be the V-d orbitals and Se-p orbitals. The Wannier-interpolated band structures are also presented in Figs. 2(c), 2(h), and 2(m) by red dashed lines, which reveal that the interpolated bands are well consistent with the DFT results. More detailed discussions can be found in Appendix B.

The calculated total and partial electronic density of states (DOSs and PDOSs) shown in Figs. 2(d), 2(i), and 2(n) are consistent with the orbital resolved energy band structures. One can see that the DOSs at the Fermi level are mainly contributed by the V-d orbitals with visible contributions from the

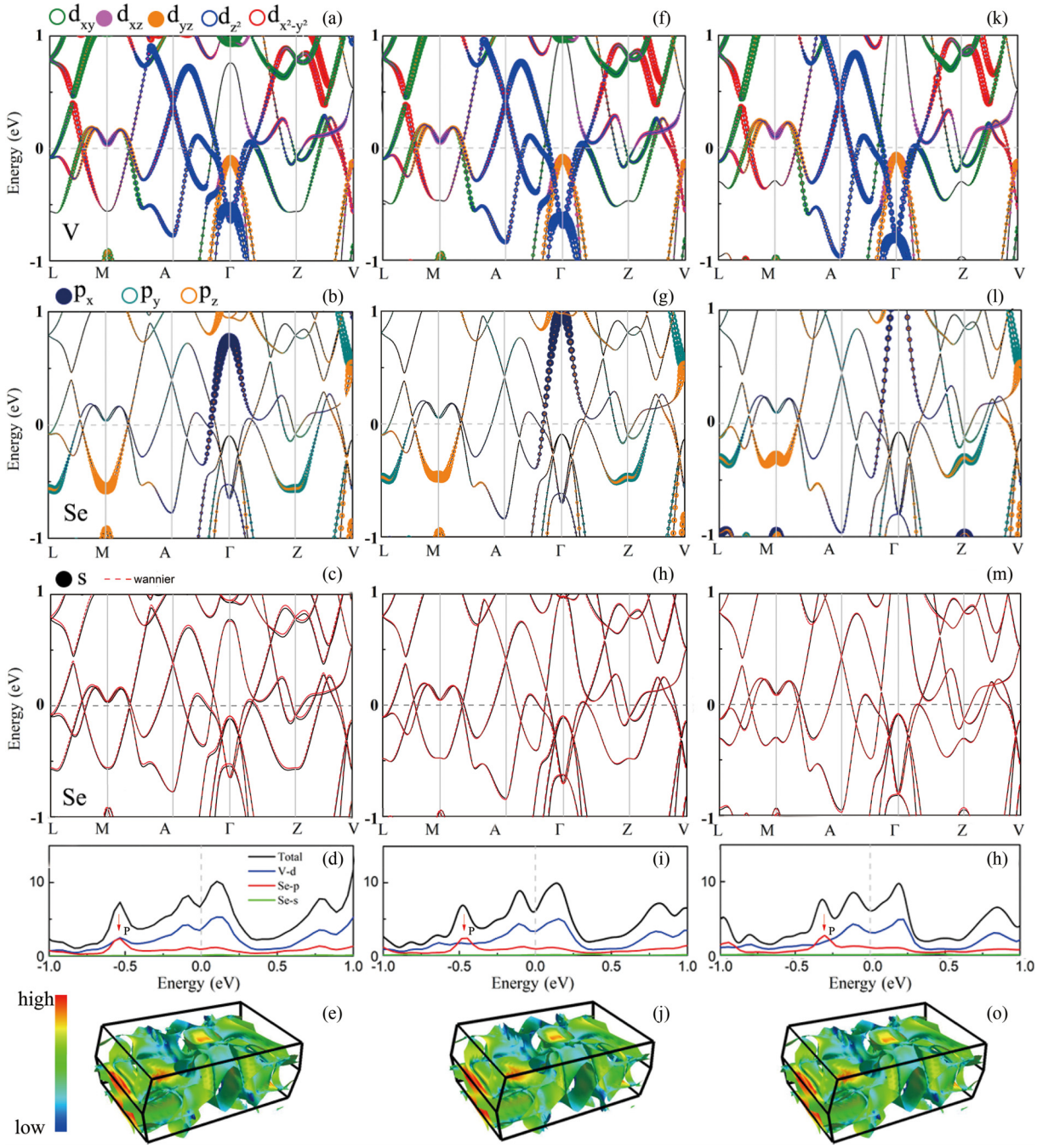

FIG. 2. Orbital-resolved band structures, corresponding total and local DOSs, and FS of 1T′-VSe_2. Panels (a–e), (f–j), and (k–o) for the pressure of 16, 22, and 35 GPa, respectively. The V-d, Se-p, and Se-s orbitals are weighted by different colors. The color bar of FS indicates the relative Fermi velocity, where the red and blue regions denote high and low Fermi velocities, respectively. The red dashed lines in the band diagrams (c), (h), and (m) are the results of Wannier fittings. The red arrows marked in panels (d), (i), and (n) indicate the peak of Se-p orbital.

Se-*p* orbitals and negligible components from the Se-*s* orbital. There are three peaks in the DOSs surrounding the Fermi level, in which two are mainly from the V-*d* orbitals and another one is dominated by the Se-*p* orbitals.

The effects of pressure are clearly revealed in the band structures as well as the corresponding DOSs. One should notice from Fig. 2 that, with increasing the external pressure, the evolution of the bands dominated by V-*d* orbitals is not obvious, only the degeneracy between A_g and B_g bands becomes weaker and weaker. While the bands dominated by Se-*p* orbitals are remarkably lifted closer to the Ferim energy as increasing the pressure. At the same time, the topology of p_y and p_z bands around the high symmetric points *M* and *Z* is modified from minima to maxima, which suggest a topological transition from electron-type band to hole-type band dominated by Se-*p* orbitals. Furthermore, the total DOS and PDOS of V-*d* orbitals at the Fermi level slightly decrease with the increase of pressure. Explicitly, $N(\epsilon_F)$ decreases from 6.63 to 5.99, and $N_{V\text{-}d}(\epsilon_F)$ decreases from 3.68 to 3.14 states/spin/Ry/unit cell as *P* increasing from 15.5 GPa to

35 GPa. However, we can clearly observe from Figs. 2(d), 2(i), and 2(n) that, with the increase of pressure, on the one hand, the peak of Se-p orbitals in PDOSs (marked by red arrow) gradually shifts toward the Fermi level, and on the other hand, the value of this peak also increases from 2.17 to 2.54, and exceeds the contribution of V-d orbitals surrounding there. This result implies that the contributions of Se-p orbitals to the SC of 1T′-VSe_2 is enhanced due to the increasing of pressure. This may be one important reason that strength of EPC boots with the increase of pressure, see the following text.

Now, let us turn to discuss the FS of VSe_2 under high pressures. Typical results of FS of 1T′-VSe_2 for $P = 16$, 22, and 35 GPa are presented in Figs. 2(e), 2(j), and 2(o), respectively. There are three bands crossing the Fermi level, which lead to intricate FSs. The hole pockets surrounding the Γ point are composed of V-d_{z^2} orbital and Se-p_x orbital, while the electron pockets around L and Z points are originated from the V-d_{xy} state. The colors on the FS denote the relative Fermi velocity.

With increasing pressure, the hole pocket along $\Gamma - Z$ line gradually disappears, while the electron pockets centering L and Z points are enlarged. Differing from the behavior of WSe_2 and $TiSe_2$ under high pressure [110,111], external high pressure includes an unusual symmetrized phase with a superlattice in VSe_2 (i.e., 1T′-VSe_2 in $C2/m$ symmetry) together with the suppression of CDW and emergence of SC. As indicated in Ref. [63], this is strongly associated with both the distortion of the structure and FS nesting. The nesting condition for the FS can be evaluated by calculating the imaginary part of the bare electronic susceptibility at low-frequency limit, whose peaks are generally pinned at the $\boldsymbol{q}$ points corresponding to Kohn anomalies in the phonon sprectrums [15,112,113]. Therefore, the physical mechanism of the pressure-dependent SC phase in symmetry $C2/m$ will be understood more indepth combining the Kohn anomalies in the phonon sprectrums which are generally driven by FS nesting. The electronic susceptibility will not be calculated for briefness herein.

C. Phonon dispersions, EPC, and SC under pressure

Figure 3 shows typical results for the phonon dispersion, projected phonon density of states (PhDOS), frequency-dependent Eliashberg spectral function $\alpha^2F(\omega)$, and cumulative frequency-dependent EPC function $\lambda(\omega)$ of 1T′-VSe_2 at high pressures of $P = 16$ GPa [Figs. 3(a1)–3(g1)], 22 GPa [Figs. 3(a2)–3(g2)], and 35 GPa [Figs. 3(a3)–3(g3)]. The unit cell of 1T′-VSe_2 contains nine atoms, which result in 27 phonon modes, comprising twenty-four optical phonon modes and three acoustic phonon modes. The acoustic branches, which are explicitly shown by the black lines in Fig. 3(a1), are crossed together with the low-energy optical branches. Its dynamical stability is justified by the absence of imaginary frequency in the low-energy zone. This is because when pressure is applied, the interatomic distances decrease, leading to a stronger bond and thus a higher spring constant. This increase in the spring constant makes the system more stable, thereby eliminating the imaginary phonon modes that signify instability within the material.

To clearly understand the contributions of V and Se atoms in the phonon spectrum, the phonon spectrum is decomposed into in-plane and out-of-plane vibrations of V and Se atoms. Furthermore, one should notice that there are four distinct Kohn anomalies in the low-energy optical branches, which are marked by Q_i with $i = 1$, 2, 3, and 4 in Fig. 3(b1). One is near the M point in the M-A direction, one localizes at the V points, and the other two are near the Γ point along the A-Γ-Z direction. All of these Kohn anomalies are predominated by the in-plane vibrations of V with nonnegligible out-of-plane vibrations of Se. As an example, the detailed discussions about the phonon spectrum of VSe_2 at $P = 16$ GPa are shown in Appendix C. The phonon spectrum will be modulated as pressure increases. This is mostly represented in the three points below. First, the out-of-plane vibration modes of V atoms always predominate in the high-frequency area as the pressure increases, extending the phonon spectrum to a higher frequency space. Second, when pressure increases, in the intermediate and low frequency zones, the vibrations of Se atoms gradually increases, but the vibration distributions of V atoms remain nearly unaltered.

This is also supported by matching variations in the projected PhDOS of V and Se. In contrast to the situation of 16 GPa in which the vibration modes and PhDOS are divided into four zones, when the pressure rises to 22GPa, the vibration modes and PhDOS may be roughly split into three zones, as illustrated in Figs. 3(a1)–3(e1) and 3(a2)–3(e2). The PhDOS of Se atoms is larger than that of V atoms in frequency area I ($0 < \omega < 250$ cm^{-1}); in frequency range II ($250 < \omega < 325$ cm^{-1}), the contributions of V and Se are almost equal; while the contributions of V atoms is larger than that of Se atoms in frequency region III ($\omega > 325$ cm^{-1}). When the pressure climbs up to 35 GPa, the vibration modes and PhDOS may be approximately divided into two frequency ranges, seeing Figs. 3(a3)–3(e3). At this situation, in frequency region I ($0 < \omega < 340$ cm^{-1}), the vibrations of Se atoms are further enhanced, such that the associated PhDOS of Se exceeds that of V atoms. In the high frequency region II ($\omega > 340$ cm^{-1}), the contribution of V atoms is also greater than that of Se atoms. The third point is that the phonon frequencies at points Q_1, Q_2, and Q_4 remain basically unchanged as the pressure increases. However, it is surprising and interesting that, unlike Q_1, Q_2, and Q_4, the phonon frequency of the Kohn anomaly at Q_3 decreases significantly with increasing pressure. Specifically, ω_{Q_3} monotonically decreases from 62.6 cm^{-1} to 52 cm^{-1} as the pressure increases from 16 GPa to 35 GPa, seeing the pink curve in Fig. 4. Differing from ω_{Q_3}, as can seen from Fig. 4, ω_{Q_i} with $i = 1$, 2, and 4 approximately equal to 75, 72, and 89 cm^{-1}, respectively. This result indicates that the greater the pressure, the more significant the phonon softening of the Kohn anomaly at Q_3.

Now, let us turn to discuss the EPC. Typical results of the Eliashberg spectral function $\alpha^2F(\omega)$ and cumulative frequency-dependent EPC function $\lambda(\omega)$ are presented in Figs. 3(g1)–3(g3). Because the acoustic and low-energy optical branches intersect with each other, there is no gap in the phonon spectrum, making it difficult to make a clear distinction in the Eliashberg spectral function $\alpha^2F(\omega)$ between acoustic and optical phonon modes. As indicated by the phonon dispersions weighted by the magnitude of

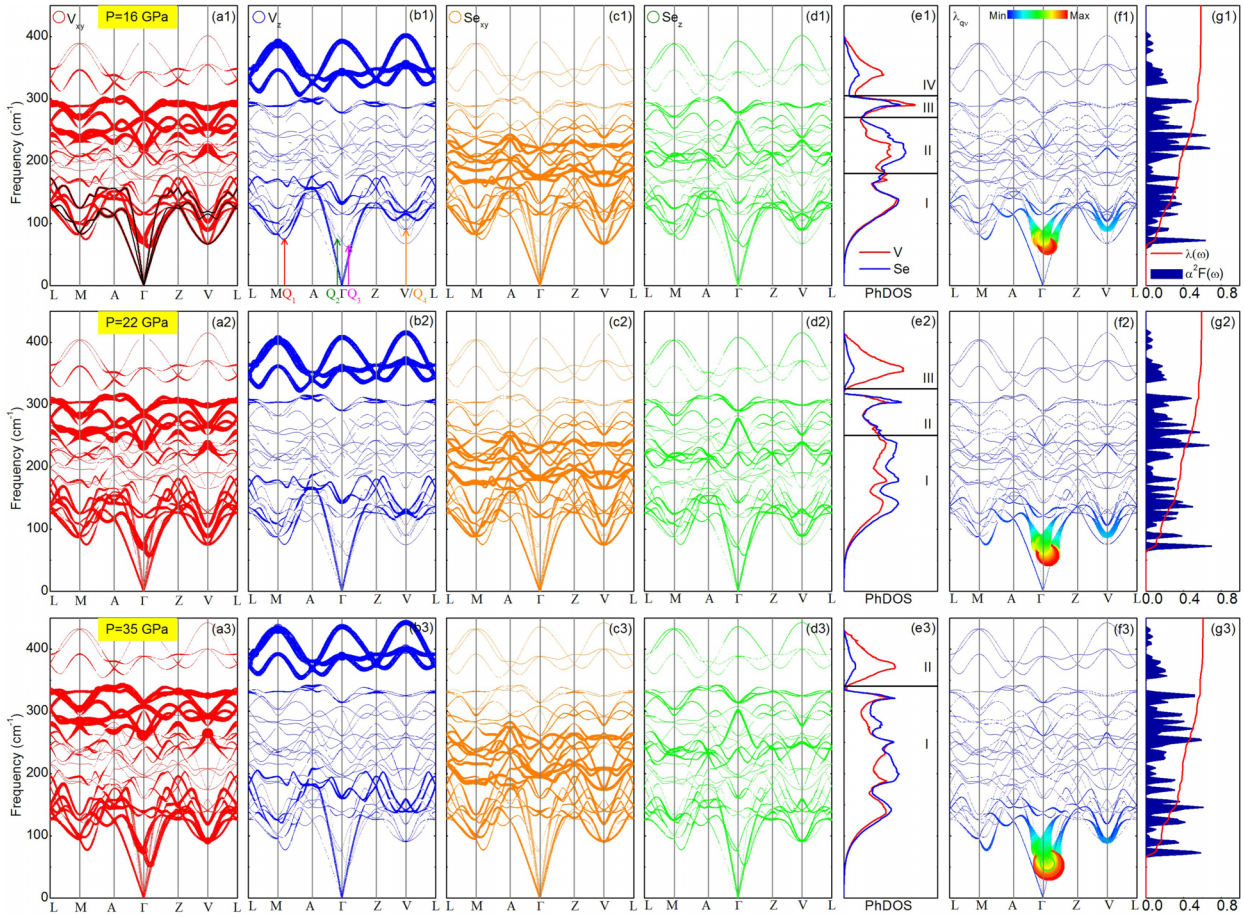

FIG. 3. Phonon dispersions weighted by the vibration modes of V and Se atoms of 1T′-VSe_2 under 16 GPa (a1–d1), 22 GPa (a2–d2), and 35 GPa (a3–d3). The red, blue, orange, and green circles represent the in-plane vibration of V, out-plane vibration of V, in-plane vibration of Se, and out-plane vibration of Se, respectively. The acoustic branches are distinguished by black curves in (a1). Four distinct Kohn anomalies in the low-energy optical branches are marked by Q_i with $i = 1, 2, 3$, and 4 in Fig. 3(b1). Panels (e1), (e2), and (e3) for the PhDOS of 1T′-VSe_2 under 16 GPa, 22 GPa, and 35 GPa, respectively. The horizontal black lines in panels (e1), (e2), and (e3) guide the separation of PhDOS. Panels (f1), (f2), and (f3) for the phonon dispersions weighted by the magnitude of EPC λ_{qv} of 1T′-VSe_2 under 16 GPa, 22 GPa, and 35 GPa, respectively. Panels (g1), (g2), and (g3) for the Eliashberg spectral function $\alpha^2F(\omega)$ and cumulative frequency dependence of EPC $\lambda(\omega)$ of 1T′-VSe_2 under 16 GPa, 22 GPa, and 35 GPa.

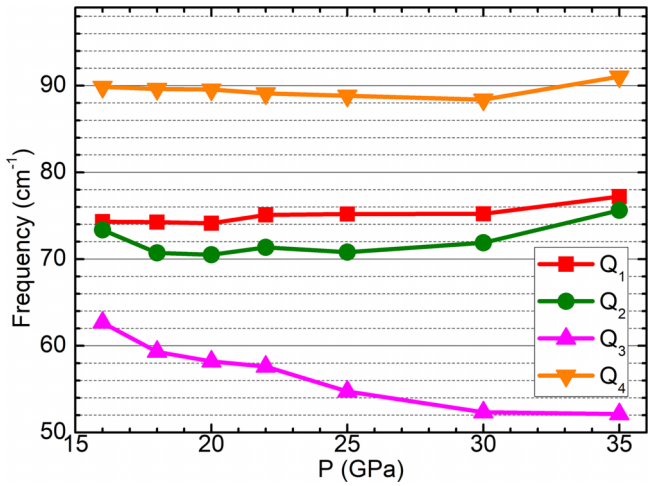

FIG. 4. (a) The variations of frequency ω_{Q_i} (in unit of cm^{-1}) as a function of pressure P (in unit of GPa). Here, Q_i with $i = 1, 2, 3$, and 4 are marked in Fig. 3(b1).

mode-resolved EPC λ_{qv} in Figs. 3(f1)–3(f3), the mode-resolved EPC λ_{qv} is mainly from the two Kohn anomalies at Q_2 and Q_3 surrounding the Γ point in the low-energy optical branches, which are dominated by the in-plane vibrations of V atoms. Therefore, combined with the analysis of the electronic structures shown above, one can carefully find that the two lowest energy peaks of the Eliashberg spectral function $\alpha^2F(\omega)$ mainly originate from the coupling between electrons in out-of-plane V-3d orbitals and in-plane vibration phonons of V atoms. More specifically, the Kohn anomaly at Q_3 donates larger contributions than that near the Q_2 point, and triggers a higher peak in $\alpha^2F(\omega)$.

Furthermore, the positions of peaks in $\alpha^2F(\omega)$ are consistent with those of the PhDOS. By this way, one can analyze the contributions of phonons in each region marked in Figs. 3(e1)–3(e3). We focus our attention on the case of 16 GPa. It is obvious that the phonons from the region I ($0 < \omega < 180$ cm^{-1}), almost equally dominated by the V and Se vibrations, make the main contributions to the cumulative frequency-dependent EPC $\lambda(\omega)$. They account for

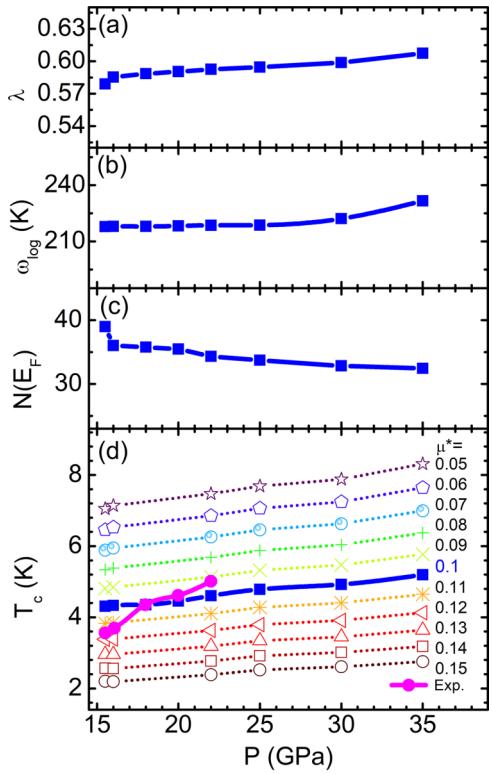

FIG. 5. The variations of (a) the total EPC λ, (b) the logarithmic mean of the phonon frequency $\omega_{\log}$,(c) electronic DOS at FS in unit of states/spin/Ry/unit cell, and (d) the SC transition temperature T_c (in unit of K) within the external pressure P (in unit of GPa), respectively. Different symbols in panel (d) are for different values of μ^*. Especially, the blue solid squares are for $\mu^* = 0.1$. The magenta solid circles in panel (d) are the experimental results of T_c [62].

approximately 60% of the total EPC intensity of $\lambda = 0.59$. The optical phonons in region II ($180 < \omega < 270$ cm^{-1}) provides approximately 28% contribution to the total λ. While the high-frequency regions III ($270 < \omega < 305$ cm^{-1}) and IV ($\omega > 305$ cm^{-1}) account for only approximately 6.5% and 5.5% of the total λ, respectively. The total EPC λ and the logarithmic mean of the phonon frequency $\omega_{\log}$ are both variables that have a direct relationship with SC transition temperature T_c according to Eq. (5). Our calculations reveal that, with increasing the pressure from 16 GPa to 35 GPa, λ slightly increases from 0.59 to 0.61 and $\omega_{\log}$ increases monotonically from 217.8 to 231.6 K, seeing Figs. 5(a) and 5(b). However, the electronic DOS at FS slightly decreases as the pressure increases, which is shown in Fig. 5(c). Such total EPC values are in favor of a weak electron-phonon SC, which is remarkably different from the situation of charge doping which will be discussed in the following text.

The value of empirical parameter $\mu^* = 0.1$ was widely used in theoretical studies of superconductors and has produced consistent results of T_c with experimental observations in various systems, as evidenced by the references [114–121]. By using this typical value of $\mu^* = 0.1$, our theoretically evaluated T_c is close to the experimental measurements [62], seeing the blue solid squares and magenta solid circles in Fig. 5(d). Furthermore,it is necessary to thoroughly examine the reliability of the model's agreement with experimental data. To address this concern, we performed a sensitivity analysis by using a range of μ^* values (0.05–0.15) for a series of pressure P. The corresponding results are also presented in Fig. 5(d). It is obvious that, for a constant pressure (empirical parameter μ^*), T_c decreases monotonically (increases slightly) with the increasing of μ^* (of P). For example, if $P = 35$ GPa ($P = 15.5$ GPa), then the largest (smallest) value of T_c is estimated as 8.3 K (2.2 K) within a choice of $\mu^* = 0.05$ ($\mu^* = 0.15$). This analysis demonstrates the dependence of T_c on μ^* and provides a more comprehensive assessment of the model's validity. Based on the above calculations and numerous relevant literature, we believe that our calculations are reasonable, and it is important to notice that $\mu^* = 0.1$ may be a good choice and has a significant impact on the calculated T_c values.

Our calculations also suggest that, as the pressure increases from 16 GPa to 35 GPa, no dome-shaped phenomenon in the pressure dependence of T_c is found, but T_c increases gently from 4.3 to 5.2 K. On one side, this no dome-shaped variation found in our calculations is in agreement with the experimental observation in Ref. [62]. On the other side, the T_c from experiments [62] shows a clear positive dependence on pressure, whereas T_c from theoretical calculations is almost constant for $P = 15$–20 GPa. This discrepancy between the theoretical calculations and experimental values of T_c can be understood from the Allen-Dynes modified McMillan Eq. (A5) shown in Appendix A, which is directly related to the electronic DOS on the FS and the phonon spectrum of the system. Our calculations reveal that the negligible dependence of calculated T_c on pressure P may be because the FS (Fig. 2) and the phonon spectrum (Fig. 3) have a relatively weak response to pressure, resulting in little influence on EPC and a relatively small change in T_c.

In addition, it is known that McMillan's approach is valid only in the regimes of validity of Migdal-Eliashberg theory. The theoretical EPC and T_c may be enhanced by taking into account the interplay between the electron-phonon interactions and other features such as the pressure-induced distortions of the atomic bonds in unit cell that locally modulate the electronic hopping, and the on-site electron-electron Coulomb repulsion that can be modeled phenomenologically as a Hubbard U term [122,123]. However, alternative forms of EPC modulated by such features are out of the scope of the present work and require more work in future. The vast majority of theoretical reports about the superconductors calculated by using the QUANTUM ESPRESSO package have not considered the Hubbard U. More importantly, we found that the T_c calculated without considering the Hubbard U is in agreement with previous experimental measurements [62], indicating the negligible effect of Hubbard correction of V-d orbitals on the EPC and T_c of VSe_2. Based on these considerations and following most of the literature, in the present work, we do not consider the Hubbard U correction in further analysis of superconducting properties of VSe_2.

The no dome-shaped response of T_c to pressure in VSe_2 is an interesting finding. To our knowledge, pressure-induced SC has been found in several TMDCs. Among all these studies, the evolution of T_c with pressure may exhibit two distinct and interesting behaviors. One scenario is that T_c attains the maximum at an optimal pressure rapidly and then drops,

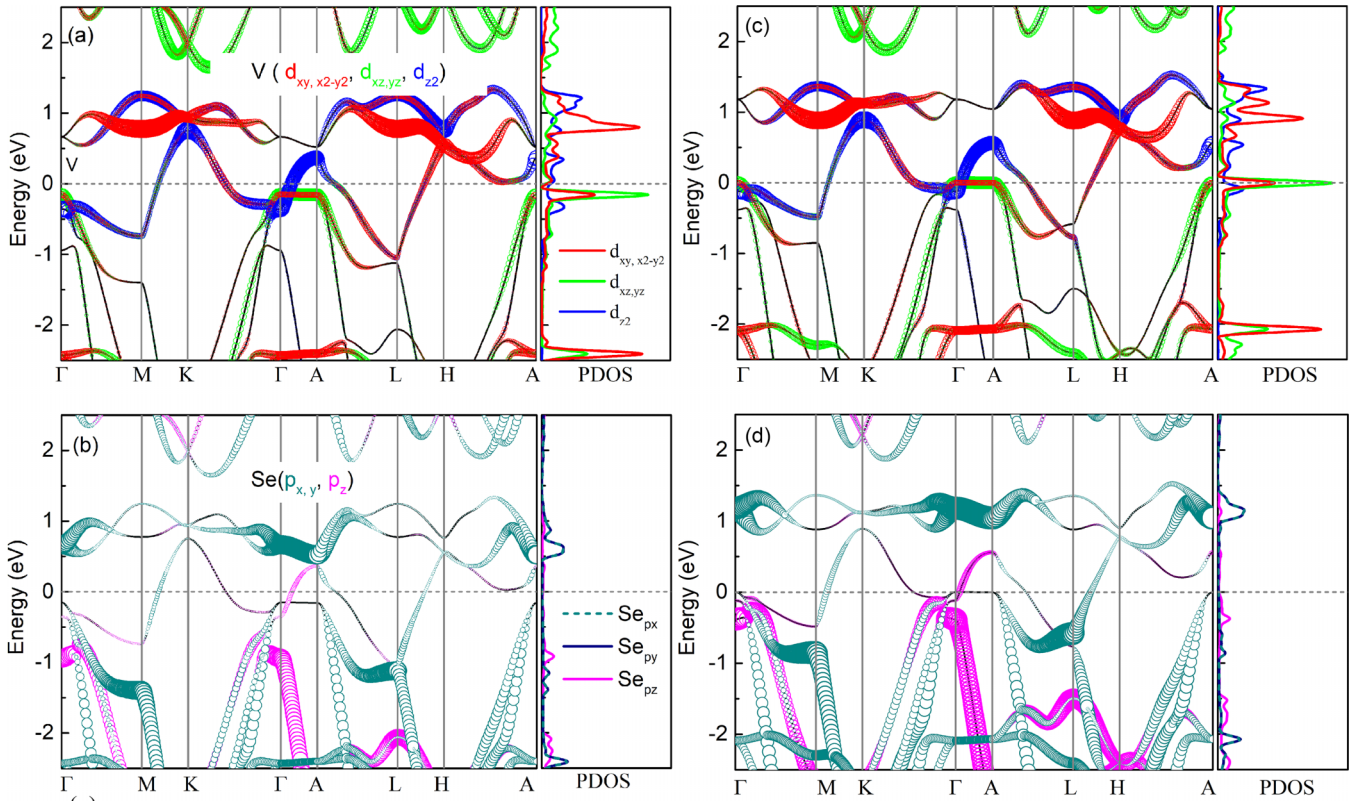

FIG. 6. Orbital-resolved band structures and the corresponding partial DOSs for 1T-VSe_2 under electron doping of $n_e = 5.14 \times 10^{21}$ cm^{-3} (a), (b), and hole doping of $n_h = -5.31 \times 10^{21}$cm^{-3} (c), (d), respectively. The red, green, and blue circles in panels (a) and (c) are for the V-d_{xy,x^2-y^2}, $d_{xz,yz}$, and d_{z^2}-orbitals of V, while the dark cyan and magenta circles in panels (b) and (d) are for the Se-$p_{x,y}$ and p_z-orbitals, respectively. The Fermi level is set to be 0 eV. The orange dashed lines in the band diagrams (b) and (d) are the results of Wannier fittings.

forming a dome-shaped behavior, which is usually driven by the suppression of the CDW state in the TMDCs due to the pressure. For example, dome-shaped SC behaviors have been observed experimentally for S-doped 2H-$TaSe_2$ [36], 2H-TaS_2 [25], 2H-$NbSe_2$ [47], 1T-$TiSe_2$ [30], 1T-$Cu_\delta TiSe_2$ [33], WTe_2 [21], and T_d-$MoTe_2$ [38], 4*Hb*-$TaSe_2$ [37], CuS_2 [71], and so on. Another scenario is that as pressure increases, T_c in certain TMDCs, such as $TaSe_2$ [34], TaS_2 [26], VSe_2 [62], WS_2 [69], and $TaTe_2$ [70], increases or decreases without a dome-shaped SC diagram, typically accompanied by structural phase transitions. Consistent with the theoretical analysis for VSe_2 in the present work, this no dome behavior of T_c may be mainly attributable to changes in DOS near FS driven by interlayer coupling enhanced by structural transitions. Besides, if the pressure is not particularly strong, then it is possible to find the coexistence between pressure-driven SC state and commensurate CDW state in some TMDCs, such as 1T-TaS_2 [20], 1T-$TaSe_2$ [34], 2H-TaS_2 and 2H-$TaSe_2$ [23], in which T_c may increase without a dome-shaped SC phase diagram. Differing from the case of pressure-induced structural transition, this T_c response to pressure might be a consequence of phonon hardening or of FS-induced changes with pressure.

IV. DOPING-DEPENDENT SUPERCONDUCTIVITY IN 1T-VSe_2

As reported in previous literature, it is a positive and available physical means by charge doping to suppress the CDW in various TMDCs and then drive the systems into a novel SC phase. However, it is unclear whether this physical regulation method is still effective for 1T-VSe_2. Compared to the pressure-dependent SC analyzed above, will charge doping bring about more interesting results? Can the EPC be enhanced by doping? Can the T_c be increased by doping? Whether there exits dome-shaped evolution of T_c with doping concentration? To address these doubts, now we turn to discuss the charge doping induced SC in 1T-VSe_2, which may be helpful to gain more thorough understanding of the physics properties of VSe_2 as well as other TMDCs.

A. Electronic structures

Typical results of orbital-resolved band structures, the corresponding partial electronic DOSs and three-dimensional FSs of charge-doping 1T-VSe_2 are presented in Fig. 6, in which the left panels 6(a) and 6(b), and right panels 6(c) and 6(d) are for e-doping with $\delta n_e = 5.14 \times 10^{21}$ cm^{-3} and h-doping with $\delta n_h = -5.31 \times 10^{21}$ cm^{-3}, respectively. It is clear from Fig. 6 that the band structures show metallic features with VB and CB crossing the Fermi level. The V-d orbitals are dominant components for conduction and valence bands, seeing Figs. 6(a) and 6(c). Furthermore, Fig. 6(b) indicates that the contributions from Se-p orbitals surrounding the FS are negligible but visible along the high-symmetric direction of Γ-A. While it is clear in Fig. 6(d) for the case of h-doping, the Fermi level is depressed, resulting in enhanced

contributions of Se-p orbitals near the FS, especially around the Γ point and along the high-symmetric directions of Γ-A and L-H.

The d_{z^2} orbital of V mainly dominates the bands crossing the Fermi level along the high symmetric directions Γ-M-K-Γ-A-L, while d_{xy} and $d_{x^2-y^2}$ orbitals mainly contribute the bands crossing the Fermi level along L-H-A. The flat band along the high-symmetric direction Γ-A is mainly originated from the orbitals d_{xz} and d_{yz}, which is consistent with the angle-resolved photo emission spectroscopy observations [94]. This flat band indicates the existence of heavy fermions and van Hove singularity. The synergy of the flat band contributes to a high density of electron gas at the Fermi level, seeing the green line in the right panels of Figs. 6(a) and 6(c), which favors conventional electron-phonon superconductors. In addition, the Wannier-interpolated band structures are also presented in Figs. 6(b) and 6(d) by orange dashed lines, which reveal that the interpolated bands are well consistent with the DFT results. More details about the band structures of VSe_2 under charge doping can be found in Appendix D.

We point out that with increasing the concentration of doped electron or hole, the evolution of the bands dominated by V-d orbitals is not obvious, but the hybridization among each sub-band may be modulated. Specially, the hybridization between band E' and band E'' along the direction Γ-A may be enhanced due to h-doping. Furthermore, the Fermi level is shifted up or down by the e-doping or h-doping, respectively.

The evolution of FS with doping concentration is shown in Fig. 7. In the case of e-doping, there is almost one band (i.e., the A_1' band including d_{z^2} orbital) crossing the Fermi level. Correspondingly, the FS exhibits elliptical-shaped arcs around K points in the BZ at a cross-section of $k_z = 0$, see Figs. 7(a)–7(f). With increasing δn_e, the evolution of FS is not significant indicating a relatively weak change of electronic DOS at FS which plays an important role for SC properties. While for the case of h-doping, there are two bands crossing the Fermi level if the concentration of the doped hole is large enough, see Figs. 7(g)–7(m). As a result, the FS of h-doping VSe_2 is divided into two regions. The outer region is the same as that of e-doping, but the inner region is characterized by a circle-shaped hole pocket which arises from the flat band along the Γ-A direction. With increasing δn_h, differing from the case of e-doping, the evolution of FS (especially the inner circle-shaped hole pocket) is significant indicating relatively strong change of electronic DOS at FS which may cause remarkable modulation of SC properties (see the following discussions). In addition, the red, green, and blue regions of FS in Fig. 7 indicate high, middle, and low Fermi velocity on the FS, which reflect different slopes of the bands. Thus, the hole pocket surrounding Γ point has a lower Fermi velocity. In the outer region of FS, the high velocity of the FS concentrates on the boundary of the BZ, while the low velocity is mainly surrounding the concave angles along the Γ-K direction.

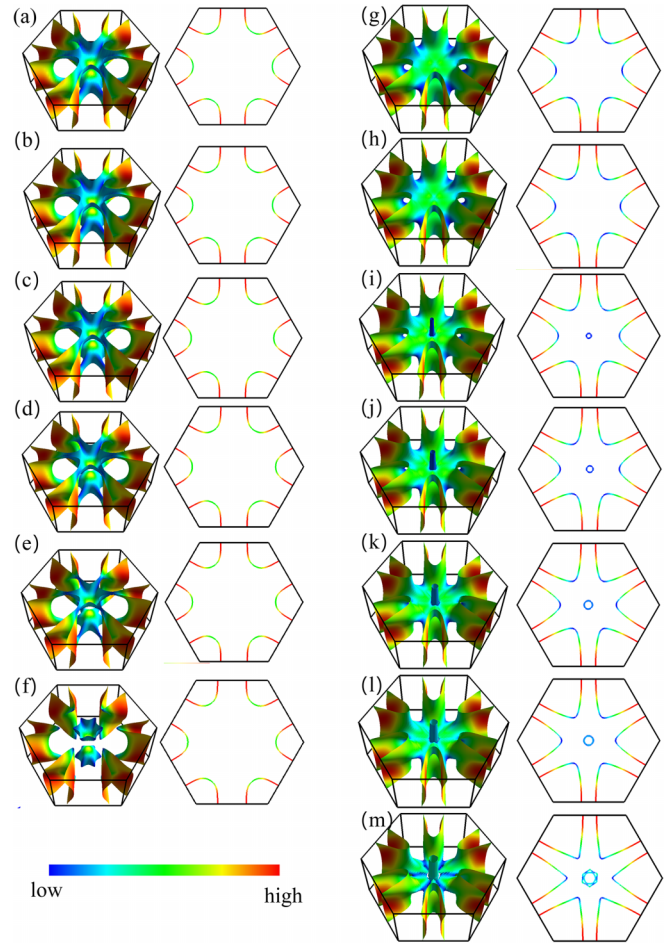

FIG. 7. The FSs for 1T-VSe_2 under various e-doping concentration of $n_e = 4.64$, 5.14, 5.64, 5.97, 6.47, and 7.46 (in unit of 10^{21} cm^{-3}) (a)–(f), and under various h-doping concentration of $n_h = -4.64$, −5.14, −5.97, −6.47, −7.13, −7.46, and −8.47 (in unit of 10^{21} cm^{-3}) (g)–(m). The red, green, and blue regions of FSs indicate high, middle, and low Fermi velocities v_F, respectively.

B. Phonon dispersions, EPC, and SC of 1T-VSe_2 under charge doping

The results of phonon of 1T-VSe_2 under charge doping are represented in Fig. 8. In Fig. 8(a), we show the phonon spectrum of 1T-VSe_2 without doping. Consistent with the previous reports, there exist Kohn anomalies and imaginary frequencies in the lowest acoustic branch, seeing the green curve in Fig. 8(a). These imaginary frequencies suggest a $4 \times 4 \times 3$ CDW phase in 1T-VSe_2, which has been extensively discussed in other literatures, such as Ref. [93]. The lowest points of these imaginary frequencies corresponding to the Kohn anomalies are also marked by gray arrows and denoted by Q_i with $i = 1, 2,..., 6$. The instability of the high symmetry structure known as phonon is directly linked to the CDW distortion. Therefore, a phonon dispersion without an imaginary frequency indicates that the structure is stable compared to the CDW structure.

Like applying external pressure, charge doping is also an effective means of eliminating the CDW states. As shown in Fig. 7, doping electrons or holes into the system shrinks the original electron pockets of FS around the K point. Moreover, a lower-energy band starts to cross E_F, forming a 3D hole pocket around Γ point. Additional doping of charge carriers such as electrons or holes can result in filling electronic states that were previously empty, leading to a more stable electronic configuration that positively affects the lattice. When

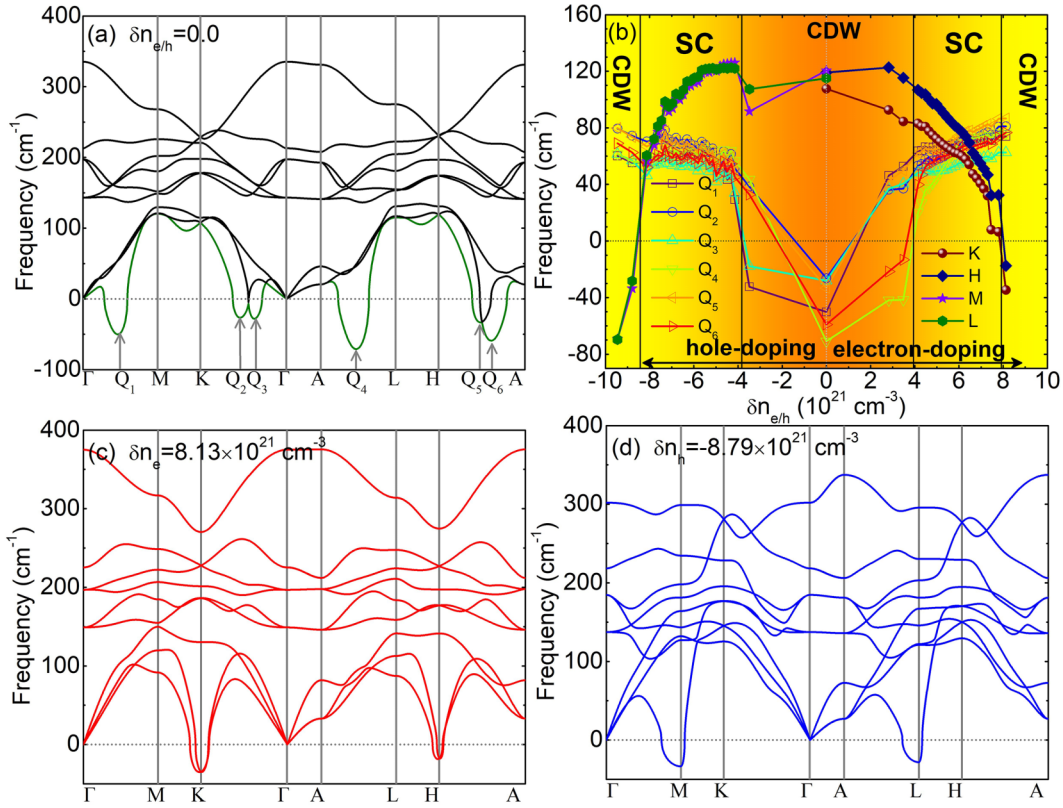

FIG. 8. (a) Phonon spectrum of intrinsic 1T-VSe_2, in which the imaginary frequencies at Q_i with $i = 1, 2, ..., 6$ are marked by gray arrows. (b) The variations of phonon frequencies at Q_i marked in panel (a) and at high symmetric points K, H, M, and L with the concentration of e- and h-doping $\delta n_{e/h}$ (in unit of 10^{21} cm^{-3}). Three different CDW phases and two different SC phases corresponding to different charge doping regions are indicated by black vertical lines and color background. (c) Phonon spectrum of 1T-VSe_2 under the e-doping $\delta n_e = 8.13 \times 10^{21}$ cm^{-3}. (d) Phonon spectrum of 1T-VSe_2 under the h-doping $\delta n_h = -8.79 \times 10^{21}$ cm^{-3}.

the charge doping level is appropriate, the CDW formation energy ($\Delta E = E_{CDW} - E_{1T}$, where E_{CDW} and E_{1T} are the total energies of the relaxed $4 \times 4 \times 3$ CDW structure and the 1T structure), becomes positive, such as $\Delta E = 28.5$ meV and 83.1 meV for the doped VSe2 with $\delta n_e = 5.14 \times 10^{21}$ and $\delta n_h = -5.14 \times 10^{21}$ h/f.u., respectively, indicating the 1T structure is more energy-stable, and the CDW of VSe_2 is not favorable in energy. This doping effect in the bulk VSe_2 can also be observed in the real-space distributions of the charge density. For example, our calculations reveal that doping one electron or one hole into a "David Star" notably decreases the charge density at the center and inner atoms of the "David Star," weakening the charge density clustering (not shown for briefness). Overall, these changes in the electronic structures caused by doping weaken the strength of EPC and suppress CDW by eliminating imaginary frequencies. Namely, proper levels of charge doping can have a positive impact on the stability of the electronic configuration, which in turn, can positively impact the lattice structure.

The variations of phonon frequencies at Q_i and high symmetric points K, H, M, and L with the concentration of electron and hole doping $\delta n_{e/h}$ are plotted in Fig. 8(b). Through a series of careful calculations of phonon, we find that, as the concentration of charge doping changes, the charge order of 1T-VSe_2 could be divided into five different regions including three CDWs and two SCs regions, which are distinguished in the colored background in Fig. 8(b). The corresponding critical concentrations of charge doping are marked with vertical black lines. Explicitly, with increasing the concentrations of electron and hole doping, i.e., δn_e and δn_h, the imaginary frequencies of Q_i gradually disappear, see the active squares, blue circles, green up-triangles, cyan down-triangles, black left-triangles, magenta right-triangles shown in Fig. 8(b). When the e- and h-doping increase from zero to the critical concentrations, $\delta n_e^c = 4.15 \times 10^{21}$ cm^{-3} and $\delta n_h^c = -4.15 \times 10^{21}$ cm^{-3}, respectively, all of the frequencies of Q_i ($i = 1, 2, ..., 6$) become positive which indicate the CDW state is suppressed. After that, the system is driven into SC states, and the corresponding concentrations of e-doping and h-doping are 4.15×10^{21} $cm^{-3} \leqslant \delta n_e \leqslant 7.80 \times 10^{21}$ cm^{-3} and -8.47×10^{21} $cm^{-3} \leqslant \delta n_h \leqslant -4.15 \times 10^{21}$ cm^{-3}, respectively. Furthermore, in the double SC regions induced by e-doping and h-doping, respectively, one can see that, on one side, the phonon frequencies at Q_i slightly increase from $\sim$40 cm^{-1} to $\sim$80 cm^{-1} as the concentration of charge doping increases; while on the other side, the phonon frequencies at high symmetric points K and H (M and L) are gradually softened from $\sim$110 cm^{-1} to $\sim$10 cm^{-1} (from $\sim$130 cm^{-1} to $\sim$20 cm^{-1}) as the concentration of e-doping (h-doping) increases, seeing the wine and navy dots (violet and olive dots) shown in Fig. 8(b). These Kohn anomalies as well as softened phonon frequencies may play a crucial role in the emergency of SC in charge doped 1T-VSe_2, which will be discussed in detail in the following text.

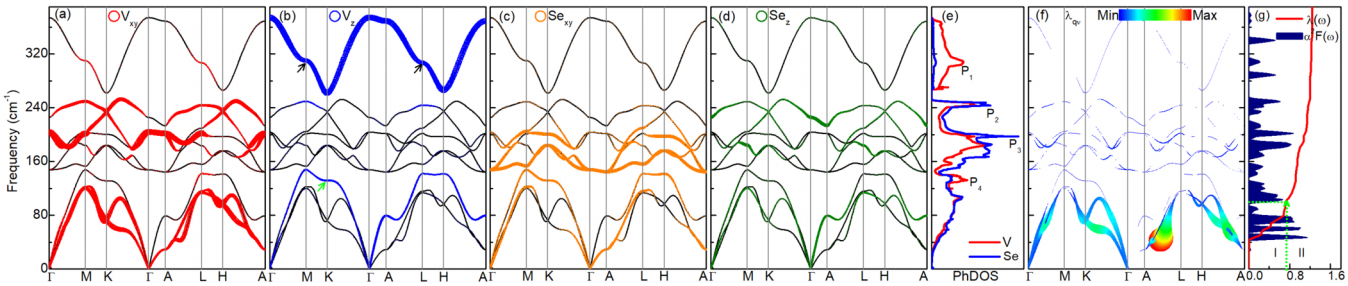

FIG. 9. (a)–(d) Phonon dispersions weighted by the vibration modes of V and Se atoms of 1T-VSe_2 under an e-doping concentration of $\delta n_e = 5.14 \times 10^{21}$ cm^{-3}. The red, blue, orange, and green circles represent the in-plane vibration of V, out-plane vibration of V, in-plane vibration of Se, and out-plane vibration of Se, respectively. The van Hove singularities in phonon are indicated by black and green arrows in panel (b). (e) The corresponding PhDOS of 1T-VSe_2. Four distinguishable peaks in PhDOS are labeled by P_i with $i = 1$, 2, 3, and 4. (f) The phonon dispersions weighted by the magnitude of EPC $\lambda_{q\upsilon}$. (g) The Eliashberg spectral function $\alpha^2F(\omega)$ and cumulative frequency dependence of EPC $\lambda(\omega)$ of 1T-VSe_2 under e-doping. The green dotted lines divide $\lambda(\omega)$ into two parts which are labeled by I and II.

Further detailed calculations indicate that for much heavier e-doping, i.e., $\delta n_e > 7.80 \times 10^{21}$ cm^{-3}, the phonon frequencies at high symmetric points K and H become imaginary. While for much heavier h-doping, i.e., $\delta n_h < -8.13 \times 10^{21}$ cm^{-3}, the phonon frequencies at high symmetric points M and L become imaginary. Additionally, phonon dispersions for $\delta n_e = 8.13 \times 10^{21}$ cm^{-3} and $\delta n_h = -8.79 \times 10^{21}$ cm^{-3} are shown in Figs. 8(c) and 8(d), respectively. These results suggest that new CDW states may occur in VSe_2 with heavier charge doping, which will not be discussed in depth since it is out of the scope of the present work. However, we hope that these new CDW states could be confirmed in the future experiments.

In Figs. 9 and 10, we show the typical results for the projected phonon dispersions, PhDOS, frequency-dependent Eliashberg spectral function $\alpha^2F(\omega)$, and cumulative frequency-dependent EPC function $\lambda(\omega)$ of 1T-VSe_2 under electron and hole doping concentrations of $n_e = 5.14 \times 10^{21}$ cm^{-3} and $n_h = -5.14 \times 10^{21}$ cm^{-3}, respectively. It is clear to us that there are nine phonon modes since the unit cell of 1T-VSe_2 contains three atoms. Its dynamical stability is justified by the absence of imaginary frequency in the low-energy zone. The detailed discussions about the phonon dispersions as well as the corresponding PhDOS shown in Figs. 9 and 10 are presented in Appendix E.

In the following text, we discuss charge doping induced SC properties of 1T-VSe_2. Typical phonon dispersions weighted by the magnitude of mode-resolved EPC $\lambda_{\boldsymbol{q}\nu}$ are shown in Figs. 9(f) and 10(f), which correspond to the e-doping and h-doping with concentration of $n_e = 5.14 \times 10^{21}$ cm^{-3} and $n_h = -5.14 \times 10^{21}$ cm^{-3}, respectively. The corresponding results of the Eliashberg spectral function $\alpha^2F(\omega)$ and cumulative frequency-dependent EPC function $\lambda(\omega)$ are plotted in Figs. 9(g) and 10(g).

First, we analyze the results of e-doping. We can see from Fig. 9(f) that the mode-resolved EPC $\lambda_{\boldsymbol{q}\nu}$ is mainly from the lowest double acoustic branches. The Kohn anomalies at Q_i $(i = 1 - 6)$ [labeled in Fig. 8(a)] as well as the high symmetric points K and H, which are dominated by the in-plane vibrations of V atoms, donate larger contributions. Especially, the greatest contribution is generated from the Kohn anomaly at Q_4 along the high symmetry direction A-L. Therefore, although the phonons located in the energy range of $\omega < 120$ cm^{-1} almost equally dominated by the V and Se vibrations, one can carefully conclude that the four peaks of the Eliashberg spectral function $\alpha^2F(\omega)$ in this energy range mainly originate from the coupling between electrons in out-plane V-3d orbitals and in-plane vibration phonons of V atoms. Furthermore, the phonons located in the energy range of $\omega < 100$ cm^{-1} provide approximately 60% contribution to the total EPC intensity of $\lambda = 1.24$, which is divided into two parts (I and II) by the green dotted line in Fig. 9(g). While the high-frequency region II, i.e., $\omega > 100$ cm^{-1}, accounts for 40% of the total EPC.

Second, we discuss the EPC results of h-doping shown in Figs. 10(f) and 10(g). For the case of h-doping, on one side, similar to the results of e-doping, the mode-resolved EPC $\lambda_{\boldsymbol{q}\nu}$ is also mainly from the lowest double acoustic branches, and

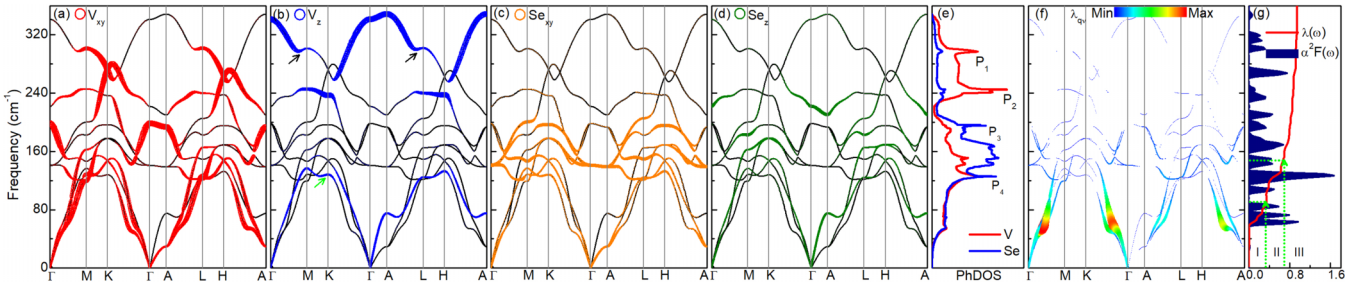

FIG. 10. Same as Fig. 9 but for the 1T-VSe_2 with h-doping concentration of $\delta n_h = -5.14 \times 10^{21}$ cm^{-3}. In (g), the green dotted lines divide $\lambda(\omega)$ into three parts which are labeled by I, II, and III.

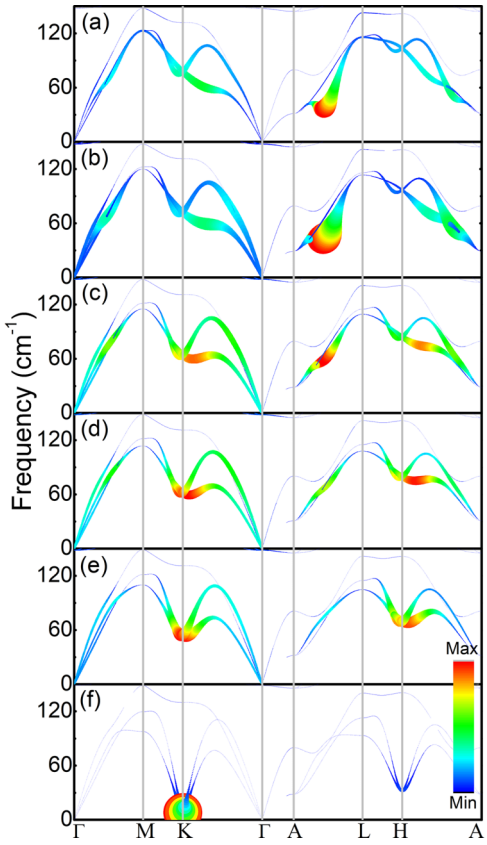

FIG. 11. (a)–(f) The acoustic branches of phonon spectrum of 1T-VSe_2 weighted by the magnitude of EPC λ_{qv} under the various e-doping concentrations of $n_e = 4.64$, 5.14, 5.64, 5.97, 6.47, and 7.46 (in unit of 10^{21} cm^{-3}). Only acoustic branches lower than 150 cm^{-1} are shown.

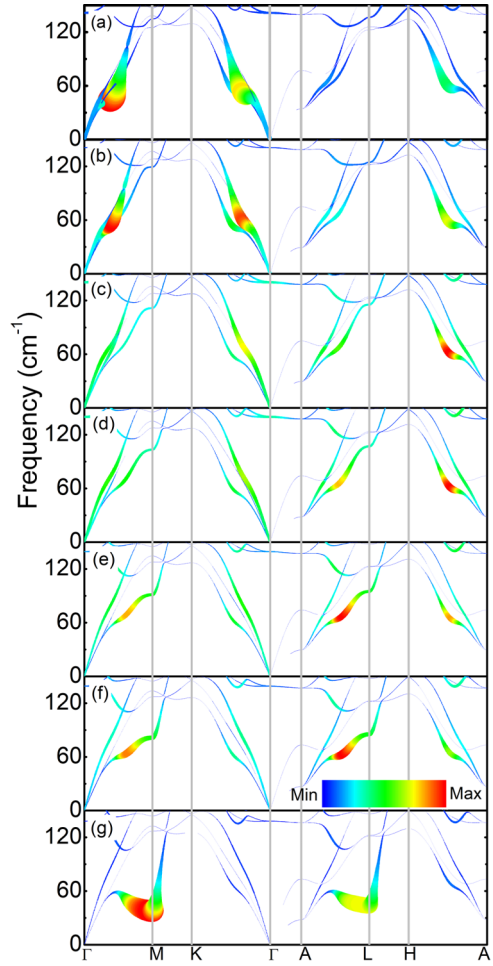

FIG. 12. (a)–(g) The phonon spectrum of 1T-VSe_2 weighted by the magnitude of EPC λ_{qv} under the various h-doping concentrations of $n_h = -4.64$, -5.14, -5.97, -6.47, -7.13, -7.46, and -8.47 (in unit of 10^{21} cm^{-3}). Only phonons with frequencies lower than 150 cm^{-1} are shown.

the Kohn anomalies at Q_i ($i = 1 - 6$) donate larger contributions; While on the other side, differing from the results of e-doping, the greatest contributions originate from the Kohn anomaly at Q_1 and Q_3. Therefore, when 1T-VSe_2 is hole doped the Eliashberg spectral function $\alpha^2F(\omega)$ in the low-energy range also mainly stem from the coupling between electrons in out-plane V-3d orbitals and in-plane vibration phonons of V atoms. Moreover, the EPC curve shown in Fig. 10(g) can be roughly divided into three steps denoted by I, II, and III therein. The steps I and II are dominated by the acoustic branches, and step III is dominated by the optical branches. The phonons located in the energy range I ($0 < \omega < 90$ cm^{-1}) provides approximately 38% contribution to the total EPC intensity of $\lambda = 0.94$. The phonons in range II, i.e., 90 cm^{-1} $< \omega <$ 150 cm^{-1}, accounts for 35% of the total λ. While the high-frequency range III only contributes 27% to the total EPC.

Third, and most importantly, we discuss the dependence of superconducting EPC of 1T-VSe_2 on the charge doping concentration. For this purpose, we plot the typical phonons weighted by the magnitude of EPC λ_{qv} for various e-doping and h-doping concentrations in Figs. 11 and 12, respectively. Only the phonons with frequencies lower than 150 cm^{-1} are shown therein. For smaller e-doping concentrations, such as $n_e = 4.64 \times 10^{21}$, and 5.14×10^{21} cm^{-3}, the maximum contribution to EPC comes from the Kohn anomaly at point Q_4, seeing Figs. 11(a) and 11(b). As the concentration of e-doping increases, the phonons of these points Q_i are gradually hardened, while the phonons at high symmetry points K and H undergo significant softening. From Figs. 11(c)–11(e) which are for $n_e = 5.64 \times 10^{21}$, 5.97×10^{21}, and 6.47×10^{21} cm^{-3}, we can see that the contribution at point Q_4 becomes weaker and weaker, while the contributions near the high symmetry points K and H become stronger and stronger since the Kohn anomalies at K and H grow more and more remarkable. As the e-doping increases to much heavier condition, such as $n_e = 7.46 \times 10^{21}$ cm^{-3}, the mode-resolved EPC λ_{qv} entirely stem from the K point; see Fig. 11(f). For the case of h-doping, the modulation of h-doping to the phonon weighted by λ_{qv} seems more complex. From Fig. 12, one can see that as h-doping concentration increases from $n_h = -4.64 \times 10^{21}$ cm^{-3} to -7.46×10^{21} cm^{-3} the greatest contributions to λ_{qv} gradually change from point Q_1 to point Q_3, then to point Q_6, subsequently to point Q_4, and finally to the high symmetry points M and L. To sum up, after various calculations, we find that if the charge doping concentration is small the contribution to

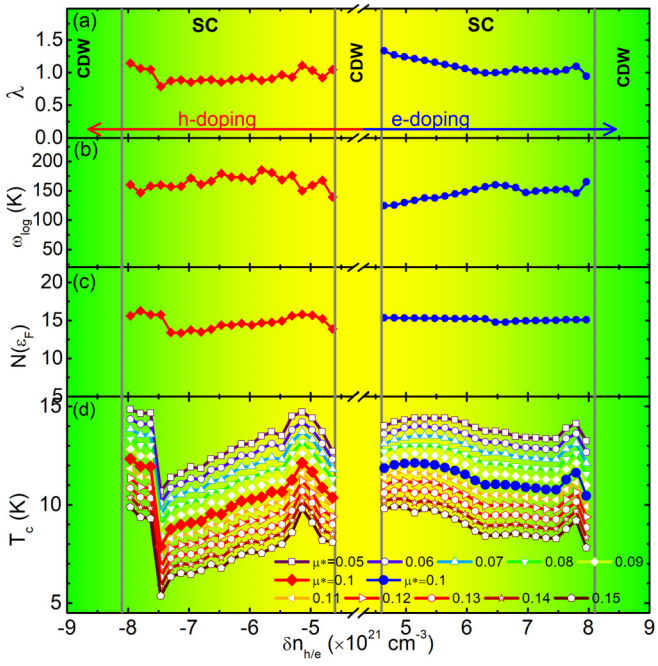

FIG. 13. The variations of (a) the total EPC λ, (b) the logarithmic mean of the phonon frequency $\omega_{\log}$ in unit of K, (c) electronic DOS at FS $N(\epsilon_F)$ in unit of states/spin/Ry/unit cell, and (d) the SC transition temperature T_c in unit of K of 1T-VSe_2 with the h-doping e-doping concentration δn_h (negative) δn_e (positive) in unit of 10^{21} cm^{-3}, respectively. The CDW regions are marked by color background. The red diamonds and blue dots are for $\mu^* = 0.1$.

EPC dominantly comes from the Kohn anomaly at points Q_i ($i = 1 - 6$). As the concentration of charge doping increases, new-type Kohn anomaly behaviors at high symmetry points (i.e., M and H for e-doping, or K and L for h-doping) are attracted and play a leading role in the superconducting EPC instead of that at the points Q_i.

Consistent with the phonon frequencies shown in Fig. 8(b), the results of calculated total EPC λ, logarithmic mean of the phonon frequency $\omega_{\log}$, electronic DOS at FS $N(\epsilon_F)$, and SC transition temperature T_c of 1T-VSe_2 for various e-doping and h-doping concentration δn_e and δn_h are shown in Fig. 13. The right panels are for e-doping while the left panels are for h-doping. With increasing δn_e from 4.48×10^{21} cm^{-3} to 6.47×10^{21} cm^{-3}, on one side, λ slightly decreases from 1.33 to 1.0. With further increasing δn_e, the variation of λ is insignificant, almost keeping at 1.0; see Fig. 13(a). Such total EPC values, which are about twice times of the situation of pressure induced, are in favor of a moderate strength EPC superconductor with higher T_c. On the other side, the logarithmic mean of the phonon frequency $\omega_{\log}$ increases monotonically from 100 K to 160 K, and then $\omega_{\log}$ changes around 150 K, see Fig. 13(b). However, the electronic DOS at FS $N(\epsilon_F)$ nearly keeps at 15 states/spin/Ry/unit cell in this e-doping concentration region, which is shown in Fig. 13(c).

The corresponding results of T_c are represented in Fig. 13(d) with empirical parameter $\mu^* = 0.1$. It is clear that T_c induced by e-doping is about twice times of that induced by pressure. As the e-doping concentration increases, T_c slightly increases from 11.6 K to 12.1 K and then gradually decreases to 10.8 K forming a small dome, which may be driven by the suppression of the CDW state in 1T-VSe_2 due to the e-doping. Subsequently, T_c suddenly increases to 11.6 K leading to another weak dome near the heavier e-doping boundary. Differing from the former case of e-doping induced the suppression of original CDW states, this type response of T_c to heavier e-doping may be a consequence of the enhancement of Kohn anomalies at high symmetric points K and H. In addition, one should notice that, however, the double dome-shaped variation of T_c with δn_e seems insignificant. This may be because although the response of phonon (especially the low-energy acoustic branches) to δn_e is remarkable, the response of FS to δn_e is relatively unremarkable, which leads to a weak influence on EPC and a relatively smaller change in T_c.

The modulation of SC transition temperature T_c via h-doping are represented by red diamonds in Fig. 13(d). The varying tendency of T_c with δn_h is nearly symmetrical with the way T_c changes with δn_e. It is clear in Fig. 13(d) that there exists a distinct dome in the variation of T_c with δn_h. Explicitly, T_c increases from 10 to 12 K as δn_h increases from -4.48×10^{21} cm^{-3} to -5.14×10^{21} cm^{-3}, and subsequently decreases to 8 K as δn_h increases ulteriorly from -5.14×10^{21} cm^{-3} to -7.46×10^{21} cm^{-3}. This dome-shaped dependence of T_c on δn_h is also driven by the suppression of the CDW state in 1T-VSe_2 due to the h-doping. Furthermore, T_c suddenly increases to 12.3 K leading to another observable dome near the heavier h-doping boundary, which is because of the enhancement of Kohn anomalies at high symmetric points M and L. The impact of T_c to δn_h is more notable compared to e-doping. This is due to the significant response of phonon and changes in FS caused by δn_h, which have distinct influences on EPC, $\omega_{\log}$, and $N(\epsilon_F)$. As a result, T_c undergoes a relatively larger change. Figure 13 also shows that with increasing δn_h from -4.48×10^{21} cm^{-3} to -7.96×10^{21} cm^{-3}, the total EPC λ marginally varies within the range of 0.85 to 1.11, $\omega_{\log}$ changes within the range of 150 to 180 K. Especially, clearly different from the case of e-doping, as δn_h increases, $N(\epsilon_F)$ alters within the range of 13.47 to 15.78 (in unit of states/spin/Ry/unit cell), whose varying tendency is well consistent with that of T_c; see Figs. 13(c) and 13(d). In addition, we also check the dependence of T_c on μ^* for various e-doping and h-doping concentrations. The corresponding results are represented in Fig. 13(d), in which the value of μ^* is tuned in the range of 0.05–0.15. One can see that for smaller μ (larger μ) the highest T_c (lowest T_c) may be 15 K (5 K).

Exploring potential candidates with high T_c among numerous TMDCs has become a research hotspot in condensed matter physics. Intrinsic 2M-WS_2 is the TMDC material experimentally confirmed to maintain the highest superconducting transition temperature record that $T_c = 8.8$ K without any external regulation [65,67]. Furthermore,the T_c of intrinsic 2H-$NbSe_2$ is measured as 7.3 K [43,46], while the T_c of most TMDCs with SC properties ranges from 2 to 4 K. Chemical doping is an effective means of regulating CDW and SC properties. It not only affects the lattice constant of the material but also causes changes in carrier concentration, the electron DOS, and other electronic parameters near the FS, resulting in changes in the EPC strength and T_c of the system. Because ion-intercalation may introduce e- or h-doping

effects in intrinsic materials, a larger cation radius can make e-doping more effective since the electrons in the outermost shell bind more loosely. Additionally, element substitution in TMDCs may also induce a charge doping effect, leading to changes both in the electronic structures and EPC of the system. Therefore, it is of scientific significance to compare and analyze the SC properties induced by charge doping and ion-intercalation in TMDCs.

Interestingly, we found that charge doping-dependent T_c exhibits a weak double-dome phenomenon with the evolution of e- or h-doping concentration. This double-dome phenomenon has not been found in any other ion-intercalated (or charge-doped) TMDCs. It is often reported that T_c decreases with an increase in the concentration of intercalated ions in TMDCs, but the decay patterns are not universal, but specific. For example, extensive studies have shown that the T_c of $NbSe_2$ with metal atom intercalation decreases with increasing ion concentration. Specifically, the T_c of Cu-embedded in $NbSe_2$ exhibits unusual *S*-type behavior [52]; the T_c of $NbSe_2$ intercalated with Li, Fe, and Ga exhibits a monotonically decreasing behavior [44,45,48]; the T_c of Rb-intercalated $NbSe_2$ shows a rapid decrease in *L*-type [55]; however, the effect of Mg-intercalation on the T_c of $NbSe_2$ is very weak [58]. Contrary to the situation with $NbSe_2$, the SC of S-doped $MoTe_2$ is enhanced and a weak dome phenomenon is observed [39]. The T_cs of Ta-doped $MoTe_2$ and Na-intercalated TaS_2 increase with increasing the concentration of Ta and Na [19,42]. In addition, the self-embedding caused by the ionic liquid gate of $PdTe_2$ leads to the occurrence of SC in $PdTe_2$ [72]. These results are completely different from the weak double dome phenomenon found in this article.

However, this work theoretically predicts that charge doping leads to a T_c of VSe_2 between $9-12$ K, which is significantly higher than the T_c of other TMDCs. Previous studies have confirmed that ionic liquid gating [72] and electrostatic gating [12] methods can reversibly modulate the carrier density of the system, thereby achieving the goal of enhancing or weakening SC induced by electron or hole doping. Under the current experimental conditions of condensed matter physics, the charge doping concentration in 2D films can reach 10^{25} cm^{-2}, and the charge doping concentration in 3D materials can reach 10^{21} cm^{-3}. Therefore, the charge doping concentration considered in this article is reasonable and experimentally feasible. Our findings reveal the possibility of regulating 1T-VSe_2 SC by manipulating the carrier charge of the material.

V. CONCLUSION

In conclusion, we have calculated and signalized in detail the SC of VSe_2 regulated by pressure and charge doping. It's essential to have a productive discussion and effectively summarize the unique and common impacts of applied pressure and charge doping on the SC of VSe_2. It is noteworthy that both methods lead to the emergence of SC by suppressing the intrinsic CDW state of the system. However, there is a subtle difference between the two approaches. Under external pressure, the system undergoes a structural phase transition, while charge doping does not cause any such transition. From the perspective of electronic structures, it is found that the $3d$ orbitals of V dominate the electron DOS near the FS, while the contribution of the $4p$ orbitals of Se is almost negligible, whether the material is under pressure or charge doping. Notably, under pressure, there is no significant effect on the shape of the FS and the DOS on the FS. However, e- and h-doping generate a flat band near the FS, with h-doping having a more profound effect on the FS shape and the corresponding electronic DOS of the system. In terms of phonons, both external pressure and charge doping can cause significant Kohn anomalies in the in-plane vibration of V atoms at certain suitable Q-points, contributing significantly to the EPC. It is worth mentioning that the Q-point of the system phonon Kohn anomaly does not change with the change of pressure, but it changes with the change of charge doping concentration. The electronic structures, FS, and phonon spectrum react differently to pressure and charge doping, which in turn affects the strength of λ and T_c. The calculations reveal that within the considered pressure range, the system exhibits weakly coupled BCS SC, and the calculated T_c agrees with prior experimental results. Notably, there is no evidence of the dome phenomenon as the pressure increases. Moreover, within the considered range of charge doping, the system displays a moderately coupled SC state, and charge doping-dependent T_c is as high as 9 to 12 K, which is about twice that of the pressure-regulated T_c. Additionally, as the doping concentration changes, T_c exhibits the dome phenomenon. To sum up, based on the analysis of electronic structures and phonon vibrations, it can be constructively concluded that the coupling between the $3d$ electrons of V and the in-plane vibration modes of V atoms plays a crucial and decisive role in the SC of VSe_2. These findings can provide valuable insights into the design and development of new materials with enhanced SC through the strategic manipulation of electronic and phononic properties.

ACKNOWLEDGMENTS

This work was supported by the National Natural Science Foundation of China (Grants No. 12175023, No. 12375234, No. 92265104, No. 12022413, No. 11674331, No. 12104458, and No. 12264032), the National Key R&D Program of China (Grant No. 2022YFA1403200), the Basic Research Program of the Chinese Academy of Sciences Based on Major Scientific Infrastructures (Grant No. JZHKYPT-2021-08), the CASHIPS Director's Fund (Grant No. BJPY2023A09), the "Strategic Priority Research Program (B)" of the Chinese Academy of Sciences (Grant No. XDB33030100), and the Major Basic Program of Natural Science Foundation of Shandong Province (Grant No. ZR2021ZD01). A portion of this work was supported by the High Magnetic Field Laboratory of Anhui Province, China.

APPENDIX A: DETAILS OF THE COMPUTATIONAL METHODS

Here, we provide the details of the computational methods employed in this work. Electron wave functions used in the DFT calculations are expanded in plane waves up to a cutoff energy of 100 Ry, and the charge density cutoff is 400 Ry. A Methfessel-Paxton smearing method with a smearing

parameter of $\sigma = 0.005$ Ry is employed. All structures are fully relaxed until the Hellmann-Feynman force acting on each atom is less than 10^{-4} Ry/Å, and the convergence criterion for self-consistent calculations is set to be 10^{-5} Ry.

Considering the 2D layered structure of the bulk VSe_2, the vdW corrections of DFT-D2 proposed by Grimme are used. The Brillouin zone (BZ) is segmented by a $36 \times 36 \times 18$ Monkhorst and Pack (MP) grid k-mesh for undistorted trigonal symmetry 1T-VSe_2, while a $10 \times 10 \times 15$ MP grid k-mesh is used for the high-pressure monoclinic symmetry VSe_2. The phonon dispersion curves and EPC are calculated within the framework of density functional perturbation theory (DFPT) [100] on a $4 \times 4 \times 2$ ($2 \times 2 \times 3$) q-mesh for the undistorted trigonal symmetry 1T-VSe_2 (high-pressure monoclinic symmetry VSe_2) using the Phonon module in the QUANTUM ESPRESSO package. A denser $72 \times 72 \times 36$ ($30 \times 30 \times 45$) MP grid k-mesh is used for the EPC calculation for undistorted structures of 1T-VSe_2 (high-pressure structures of VSe_2).

Charge doping is simulated by adding or removing electrons to the unitcell of 1T-VSe_2 with a compensating uniform charge background of opposite sign. The level of doped carriers per volume is expressed as $\delta n = n - n_0$ (cm^{-3}) with $n_0 = 5.8073 \times 10^{23}$ cm^{-3} being the intrinsic valence electron density, and positive and negative values representing e-doping and h-doping states, respectively.

Based on the Migdal-Eliashberg theory [102,103], the EPC $\lambda_{\boldsymbol{q}\nu}$ of phonon mode ν with momentum $\boldsymbol{q}$ is given by

$$\lambda_{\boldsymbol{q}\nu} = \frac{\gamma_{\boldsymbol{q}\nu}}{\pi \hbar N(\epsilon_F)\omega^2_{\boldsymbol{q}\nu}}, \tag{A1}$$

where $\omega_{\boldsymbol{q}\nu}$ is the phonon frequency, $N(\epsilon_F)$ is the electronic density of states (DOS) at the Fermi level ϵ_F, and $\gamma_{\boldsymbol{q}\nu}$ represents the phonon linewidth arising from the electron-phonon interactions. Here, $\gamma_{\boldsymbol{q}\nu}$ is written as

$$\gamma_{\boldsymbol{q}\nu} = \frac{2\pi\omega_{\boldsymbol{q}\nu}}{\Omega_{\mathrm{BZ}}} \sum_{\boldsymbol{k},n,m} \left|g^{\nu}_{\boldsymbol{k}n,\boldsymbol{k}+\boldsymbol{q}m}\right|^2 \delta(\epsilon_{\boldsymbol{k}n} - \epsilon_F)\delta(\epsilon_{\boldsymbol{k}+\boldsymbol{q}m} - \epsilon_F), \tag{A2}$$

where Ω_{BZ} denotes the volume of the BZ, $\epsilon_{\boldsymbol{k}n}$ and $\epsilon_{\boldsymbol{k}+\boldsymbol{q}m}$ are the Kohn-Sham eigenvalues, and $g^{\nu}_{\boldsymbol{k}n,\boldsymbol{k}+\boldsymbol{q}m}$ represents the electron-phonon matrix element [104]. And then, the Eliashberg electron-phonon spectrum function can be expressed as

$$\alpha^2F(\omega) = \frac{1}{2\pi N(\epsilon_F)} \sum_{\boldsymbol{q},\nu} \frac{\gamma_{\boldsymbol{q}\nu}}{\omega_{\boldsymbol{q}\nu}} \delta(\omega - \omega_{\boldsymbol{q}\nu}). \tag{A3}$$

The total EPC constant is calculated by integrating the Eliashberg spectral function $\alpha^2F(\omega)$

$$\lambda(\omega) = 2\int_0^{\omega} d\omega' \frac{\alpha^2F(\omega')}{\omega'}. \tag{A4}$$

The superconducting transition temperature T_c is determined from the calculated EPC constant $\lambda(\omega)$ by employing the Allen-Dynes modified McMillan equation [104]

$$T_c = \frac{\omega_{\log}}{1.2} \exp\left[-\frac{1.04(1+\lambda)}{\lambda - \mu^*(1+0.62\lambda)}\right], \tag{A5}$$

where μ^* denotes the effective screened repulsion constant, and $\omega_{\log}$ describes the logarithmically averaged phonon frequency given by

$$\omega_{\log} = \exp\left[\frac{2}{\lambda}\int_0^{\infty} d\omega \alpha^2F(\omega)\frac{\log\omega}{\omega}\right]. \tag{A6}$$

In the following calculations of T_c, μ^* is chosen as 0.1, a reasonable value of the Coulomb repulsion constant. We also estimate the dependence of T_c on μ^* ranging from 0.05 to 0.15.

APPENDIX B: DETAILED DISCUSSIONS ABOUT THE BAND STRUCTURES OF VSe_2 UNDER HIGH PRESSURE

The monoclinic symmetry (C_{2h}) splits the energy bands of V-d electrons into two categories: the A_g band, which include any combination of the orbitals $d_{x^2-y^2}$, d_{xy}, and d_{z^2}, and B_g band, which include the orbitals d_{xz} and d_{yz}. Here, A_g and B_g are the Mulliken notations for the irreducible representations of the point group of C_{2h}. The hybridizations among orbitals ($d_{x^2-y^2}$, d_{xy}, and d_{z^2}) in A_g band or among orbitals (d_{xz} and d_{yz}) in B_g band are remarkable. Furthermore, due to the lower symmetry of 1T′-VSe_2 under an applied high pressure, the hybridization between A_g band and B_g band is allowed. For examples, (i) the hybridization between d_{xy} (green) in A_g band and d_{yz} (purple) in B_g band along the $L-M$ direction and the $M-A$ direction, and (ii) the hybridization between d_{z^2} (blue) in A_g band and d_{xz} (pink) in B_g band surrounding the M point and along the high-symmetric direction of $\Gamma-Z-V$ can be clearly seen from Fig. 2.

The d_{yz} and d_{z^2} orbitals of V mainly dominate the lower VBs while the p_x orbital of Se dominates the upper VB surrounding the Γ point, respectively. The CB (VBs) around the L point are mainly contributed by d_{xy} (d_{z^2}, p_y, and p_z) orbitals. The CBs (VB) around the Z point are mainly dedicated by d_{xy} and d_{z^2} (p_y, and p_z) orbitals. The upper and lower CBs in the vicinity of the M point are mainly dedicated by the d_{xz} and d_{z^2} orbitals, and p_z orbital, respectively. The d_{yz} and p_z orbitals mainly dedicated to the VBs in the vicinity of the V point, respectively. The VB and CB encircling the A point as well as those along the direction of $A-\Gamma$ are mainly determined by the d_{z^2} orbital. Moreover, the bands along the $M-A$ direction are also mainly originated from the d_{z^2} orbital accompanied by the hybridizations with d_{xy} and d_{yz} orbitals. Away from the high symmetry point L (point V), the bands can be ascribed to the $d_{x^2-y^2}$, d_{xy}, and d_{yz} ($d_{x^2-y^2}$, d_{xy}, and d_{xz}) orbitals. Additionally, the hybridization between d_{xy} and p_y, the hybridization between $d_{x^2-y^2}$ and p_z in the CB along the $L-M$ direction, and the hybridization between d_{xy} and p_y in the VB bands along the $Z-V$ direction are remarkable, which indicate the positive participation of the Se-p orbitals in the novel superconducting properties of VSe_2 under high pressure.

Furthermore, a series of calculations of the hopping integral $t_{\alpha\beta}(\boldsymbol{R})$ in the maximally localized Wannier basis for the VSe_2 under pressure between 3d-orbitals (d_{z^2}, d_{xz}, d_{yz}, $d_{x^2-y^2}$, d_{xy}) at site $\mathbf{0}$ and 3d-orbitals of V-atom located at site $\boldsymbol{R}$ reveal two important features that, as P increasing from 16 GPa to 35 GPa, (i) the on-site energies of d_{xz} and d_{yz} orbitals change from 0.517 eV to 0.529 eV and from

0.506 eV to 0.515 eV, respectively; and (ii) the onsite hopping parameters between d_{yz} and d_{xy} changes from −0.449 eV to −0.507 eV. These values of hopping parameters are much greater than others, indicating the strong hybridization of band A_g and band B_g, which are also in good agreement with the DFT results shown in Fig. 2. In addition, the hopping integral $t_{\alpha\beta}(\boldsymbol{R})$ between 4*p*-orbital of Se atom and 3*d*-orbital of V atom are also in good agreement with the DFT results, which will not be discussed in detail because the contribution of 4*p*-orbital of Se atom at Fermi level is relatively weak.

APPENDIX C: DETAILED DISCUSSIONS ABOUT THE PHONON DISPERSION OF VSe_2 UNDER A PRESSURE OF $P = 16$ GPa

Here, let us take the case of $P = 16$ GPa as an example, seeing Figs. 3(a1)–3(g1), to understand the phonon of VSe_2 under pressure. Combined with the decomposition of phonon spectrum with respect to V and Se atomic vibrations and the PhDOS presented in Figs. 3(a1)–3(e1), the vibration modes can be approximately divided into four ranges, which are marked by black line in Fig. 3(e1). At the low-frequency range I ($0 < \omega < 180\ \mathrm{cm}^{-1}$), the acoustic branches are mainly contributed by the in-plane vibration modes of V atoms as well as the in-plane and out-of-plane vibration modes of Se atoms. In the range II of intermediate frequency ($180 < \omega < 270\ \mathrm{cm}^{-1}$), the in-plane vibrations of Se atoms predominates. It is also worth noting that the out-of-plane vibrations of Se atoms and the in-plane vibrations of V atoms also provide significant contributions, but the contribution of the out-of-plane vibrations of V atoms is very small in this range. While the frequency range III ($270 < \omega < 305\ \mathrm{cm}^{-1}$) mainly stem from the in-palne vibrations of V atoms with visible participations of out-of-plane vibrations of Se atoms and negligible components both from the out-of plane vibrations of V and the in-plane vibrations of Se atoms. Evidently, the out-plane vibration modes of the V atoms mainly occupy the high-frequency range IV ($\omega > 305\ \mathrm{cm}^{-1}$), which is consistent with the expectations from the lighter mass V relative to Se. These distributions are in good agreement with the projected PhDOS shown in Fig. 3(e1), which shows that the PhDOS of V and Se are almost equal in range I, the PhDOS of Se is larger than that of V in range II, the PhDOS of V is slightly larger than that of Se in range III, and the PhDOS of V is significantly larger than that of Se in range IV. Correspondingly, the 27 vibration modes of 1T′-VSe_2 at Γ point in the BZ at 16 GPa (not shown) are consistent with the above analysis of phonon dispersions weighted by the motion modes of V and Se atoms as well as the projected PhDOS.

APPENDIX D: DETAILED DISCUSSIONS ABOUT THE BAND STRUCTURES OF VSe_2 UNDER CHARGE DOPING

Differing from the monoclinic symmetry (C_{2h}) of 1T′-VSe_2 under high pressure, the triangular symmetry (D_{3h}) of 1T-VSe_2 splits the energy bands of V-*d* electrons into three categories: the A_1' band including d_{z^2} orbital, the E' band including any combination of the orbitals $d_{x^2-y^2}$ and d_{xy}, and the E'' band containing the orbitals d_{xz} and d_{yz}. Here, A_1', E', and E'' are the Mulliken notations for the irreducible representations of point group of D_{3h}. The different profiles between e-doping bands and h-doping bands are that, on the one hand, h-doping causes a hole pocket at the Γ point, which can also be clearly seen in Fig. 7. However, there is no hole band passing through the Fermi level at the Γ point where electrons are doped; on the other hand, the flat band doped with holes in the Γ-A direction almost falls on the Fermi level. While the flat band doped with electrons in the Γ-A direction is slightly lower than the Fermi level. Moreover, one can see from Fig. 6(a) that for the case of e-doping, the hybridization among each band A_1', E', and E'' is weak. But for the case of h-doping, seeing Fig. 6(c), the hybridization between band A_1' and band E' (band E' and band E'') becomes visible along the direction of K-Γ (Γ-A). The similarity between e-doping bands and h-doping bands may be that the entire hybridization between *d* orbital of V and *p* orbital of Se is unremarkable except of the hybridization between d_z^2 orbital and p_z orbital along the Γ-A direction. Consistent with the orbital resolved energy band structures, the DOS and PDOSs are mainly contributed by the V-*d* orbitals and the contributions from the Se-*p* orbitals are negligible, which can be seen from the right panels of Figs. 6(a), 6(b) and 6(c), 6(d). It is clear to us that the contribution of Se-*p* orbitals to the DOS at FS nearly vanishes. In addition, the Wannier fitting of hopping parameters show that, (i) the on-site energies of d_{xz} and d_{yz} orbitals are 0.414 eV and 0.553 eV for e-doping and h-doping, respectively; and (ii) the on-site hopping parameters between d_{xz} (d_{yz}) and d_{xy} ($d_{x^2-y^2}$) are −0.383 eV and −0.364 eV for e-doping and h-doping, respectively. These values of hopping parameters indicate the strong hybridization of band E' and band E'', which are in good agreement with the DFT results shown in Fig. 6. Other hopping parameters will not be discussed in detail for briefness.

APPENDIX E: DETAILED DISCUSSIONS ABOUT THE PHONON DISPERSIONS OF VSe_2 UNDER CHARGE DOPING

For the case of e-doping, the acoustic branches do not cross together with the low-energy optical branches, and a gap is opened between the top optical branch and the other phonon branches below; see Fig. 9. Moreover, one can see from Fig. 9 that the acoustic branches are contributed by the vibrations of V with significant vibrations of Se. The optical branches in the region from 150 to 200 cm^{-1} are predominated by the in-plane vibrations of Se. While the optical branches in the region 200 to 250 cm^{-1} mainly stem from the in-plane vibrations of V atoms as well as a small amount of out-plane vibration modes of Se atoms. The highest optical branch is predominately contributed by the out-plane vibrations of the V atoms.

These distributions are in good agreement with the projected PhDOS shown in Fig. 9(e), which shows that the PhDOS of V and Se are almost equal in the acoustic region ($\omega < 150\ \mathrm{cm}^{-1}$), the PhDOS of Se is slightly larger than that of V in the intermediate optical region from 150 cm^{-1} to 250 cm^{-1}, and the PhDOS of V is significantly larger than that of Se in the frequency region higher than 250 cm^{-1}. We also find that four distinguishable peaks in the PhDOS labeled by P_i with $i = 1, 2, 3$, and 4 in Fig. 9(e) are mainly contributed

by the van Hove singularities in the phonon dispersions. Explicitly, (i) peak P_1 in PhDOS origins from the van Hove singularities around points M and L in the top optical branch indicated by black arrows in Fig. 9(b); (ii) peak P_2 in PhDOS stems from the flat bands of phonon along the L-H direction; (iii) peak P_3 in PhDOS stems from the flat bands of phonon along the M-K and L-H directions; (iv) peak P_4 in PhDOS contributes from the van Hove singularity surrounding the K point in the acoustic branch indicated by green arrow in Fig. 9(b).

Differing from the case of e-doping, the h-doping lowers the frequency of phonon, causing the phonon spectrums to cross together with each other; see Fig. 10. Furthermore, for the h-doping case, the acoustic branches are dominated by the in-plane vibrations of V atoms. In addition, the in-plane vibration modes of the V atoms in the optical branches become more extended, resulting in mixing with the in-plane vibrations of the Se atoms in the low-frequency region from 120 to 220 cm^{-1}, and significant hybridizations with the out-plane vibrations of the V atoms in the high-frequency region 220 to 300 cm^{-1}. The corresponding projected PhDOS are presented in Fig. 10(e). We can observe from Fig. 10(e) that the PhDOS of V and Se are almost equal in the acoustic region ($\omega < 120$ cm^{-1}), the PhDOS of Se is larger than that of V in the intermediate optical region from 120 to 220 cm^{-1}, and the PhDOS of V is significantly larger than that of Se in the frequency region higher than 220 cm^{-1}. There also exist four distinguishable peaks in the PhDOS, which are labeled in Fig. 10(e). The peaks P_1 and P_4 are mainly contributed by the van Hove singularities illustrated by arrows in Fig. 10(b). The peaks P_2 and P_3 are mainly contributed by the flat bands located at the corresponding phonon frequencies. To further reveal the different effects of e-doping and h-doping on phonons of 1T-VSe_2, the nine vibration modes of 1T-VSe_2 at Γ point in the BZ under the e-doping and h-doping are also evaluated (not shown), indicating the relative motion of Se and V atoms. We find that the acoustic vibration modes (1–3) are mainly in-plane for e-doping and significantly enhanced out-of-plane for h-doping. Other vibration modes (4–9) are similar under both types of doping. These visualized vibration modes agree with the analysis of phonon dispersions weighted by the vibration modes of V and Se atoms and the projected PhDOS.

[1] A. H. Castro Neto, F. Guinea, N. M. R. Peres, K. S. Novoselov, and A. K. Geim, The electronic properties of graphene, Rev. Mod. Phys. **81**, 109 (2009).

[2] C.-L. Song, Y.-L. Wang, P. Cheng, Y.-P. Jiang, W. Li, T. Zhang *et al.*, Direct observation of nodes and twofold symmetry in FeSe superconductor, Science **332**, 1410 (2011).

[3] D. Liu, W. Zhang, D. Mou, J. He, Y.-B. Ou, Q.-Y. Wang *et al.*, Electronic origin of high-temperature superconductivity in single-layer FeSe superconductor, Nat. Commun. **3**, 931 (2012).

[4] E. Dagotto, Colloquium: The unexpected properties of alkali metal iron selenide superconductors, Rev. Mod. Phys. **85**, 849 (2013).

[5] A. Iqbal, P. Sambyal, and C. M. Koo, 2D MXenes for electromagnetic shielding: A review, Adv. Funct. Mater. **30**, 2000883 (2020).

[6] D. Voiry, A. Mohite, and M. Chhowalla, Phase engineering of transition metal dichalcogenides, Chem. Soc. Rev. **44**, 2702 (2015).

[7] W. Choi, N. Choudhary, G. H. Han, J. Park, D. Akinwande, and Y. H. Lee, Recent development of two-dimensional transition metal dichalcogenides and their applications, Mater. Today **20**, 116 (2017).

[8] S. Manzeli, D. Ovchinnikov, D. Pasquier, O. V. Yazyev, and A. Kis, 2D transition metal dichalcogenides, Nat. Rev. Mater. **2**, 17033 (2017).

[9] Q. Fu, J. Han, X. Wang, P. Xu, T. Yao, J. Zhong *et al.*, 2D transition metal dichalcogenides: Design, modulation, and challenges in electrocatalysis, Adv. Mater. **33**, 1907818 (2021).

[10] K. Deng, G. Wan, P. Deng, K. Zhang, S. Ding, E. Wang *et al.*, Experimental observation of topological Fermi arcs in type-II Weyl semimetal $MoTe_2$, Nat. Phys. **12**, 1105 (2016).

[11] C. Heikes, I.-L. Liu, T. Metz, C. Eckberg, P. Neves, Y. Wu, L. Hung, P. Piccoli, H. Cao, J. Leao, J. Paglione, T. Yildirim, N. P. Butch, and W. Ratcliff, II, Mechanical control of crystal symmetry and superconductivity in Weyl semimetal $MoTe_2$, Phys. Rev. Mater. **2**, 074202 (2018).

[12] E. Sajadi, T. Palomaki, Z. Fei, W. Zhao, P. Bement, C. Olsen, S. Luescher, X. Xu, J. A. Folk, and D. H. Cobden, Gate-induced superconductivity in a monolayer topological insulator, Science **362**, 922 (2018).

[13] V. Fatemi, S. Wu, Y. Cao, L. Bretheau, Q. D. Gibson, K. Watanabe, T. Taniguchi, R. J. Cava, and P. Jarillo-Herrero, Electrically tunable low-density superconductivity in a monolayer topological insulator, Science **362**, 926 (2018).

[14] Z. Wang, B. J. Wieder, J. Li, B. Yan, and B. A. Bernevig, Higher-order topology, monopole nodal lines, and the origin of large fermi arcs in transition metal dichalcogenides XTe_2 (X=Mo,W), Phys. Rev. Lett. **123**, 186401 (2019).

[15] W. Yang, C.-J. Mo, S.-B. Fu, Y. Yang, F.-W. Zheng, X.-H. Wang, Y.-A. Liu, N. Hao, and P. Zhang, Soft-mode-phonon-mediated unconventional superconductivity in monolayer 1T′-WTe_2, Phys. Rev. Lett. **125**, 237006 (2020).

[16] W. Wang, S. Kim, M. Liu, F. A. Cevallos, R. J. Cava, and N. P. Ong, Evidence for an edge supercurrent in the Weyl superconductor $MoTe_2$, Science **368**, 534 (2020).

[17] S. T. Lam, K. Y. Yip, S. K. Goh, and K. T. Lai, Suppression of both superconductivity and structural transition in hole-doped $MoTe_2$ induced by Ta substitution, Phys. Rev. Mater. **7**, 084802 (2023).

[18] M. M. Piva, L. O. Kutelak, R. Borth, Y. Liu, C. Petrovic, R. D. dos Reis, and M. Nicklas, Superconducting pairing symmetry in $MoTe_2$, Phys. Rev. Mater. **7**, L111801 (2023).

[19] L. Fang, Y. Wang, P. Y. Zou, L. Tang, Z. Xu, H. Chen, C. Dong, L. Shan, and H. H. Wen, Fabrication and superconductivity of Na_xTaS_2 crystals, Phys. Rev. B **72**, 014534 (2005).

[20] B. Sipos, A. F. Kusmartseva, A. Akrap, H. Berger, L. Forró, and E. Tutiš, From Mott state to superconductivity in 1T-TaS_2, Nat. Mater. **7**, 960 (2008).

[21] X.-C. Pan, X. Chen, H. Liu, Y. Feng, Z. Wei, Y. Zhou *et al.*, Pressure-driven dome-shaped superconductivity and electronic structural evolution in tungsten ditelluride, Nat. Commun. **6**, 7805 (2015).

[22] E. Navarro-Moratalla, J. O. Island, S. Mañas-Valero, E. Pinilla-Cienfuegos, A. Castellanos-Gomez, J. Quereda *et al.*, Enhanced superconductivity in atomically thin TaS_2, Nat. Commun. **7**, 11043 (2016).

[23] D. C. Freitas, P. Rodière, M. R. Osorio, E. Navarro-Moratalla, N. M. Nemes, V. G. Tissen *et al.*, Strong enhancement of superconductivity at high pressures within the charge-density-wave states of 2H-TaS_2 and 2H-$TaSe_2$, Phys. Rev. B **93**, 184512 (2016).

[24] Y. Kvashnin, D. VanGennep, M. Mito, S. A. Medvedev, R. Thiyagarajan, O. Karis, A. N. Vasiliev, O. Eriksson, and M. Abdel-Hafiez, Coexistence of superconductivity and charge density waves in tantalum disulfide: Experiment and theory, Phys. Rev. Lett. **125**, 186401 (2020).

[25] S. Xu, J. Gao, Z. Liu, K. Chen, P. Yang, S. Tian, C. Gong, J. Sun, M. Xue, J. Gouchi, X. Luo, Y. Sun, Y. Uwatoko, H. Lei, B. Wang, and J. Cheng, Effects of disorder and hydrostatic pressure on charge density wave and superconductivity in 2H-TaS_2, Phys. Rev. B **103**, 224509 (2021).

[26] Q. Dong, Q. Li, S. Li, X. Shi, S. Niu, S. Liu *et al.*, Structural phase transition and superconductivity hierarchy in 1T-TaS_2 under pressure up to 100 GPa, npj Quantum Mater. **6**, 20 (2021).

[27] T. Agarwal, C. Patra, A. Kataria, R. R. Chowdhury, and R. P. Singh, Quasi-two-dimensional anisotropic superconductivity in Li-intercalated 2H-TaS_2, Phys. Rev. B **107**, 174509 (2023).

[28] T. Luo, M. Zhang, J. Shi, and F. Zheng, Emergent charge density wave featuring quasi-one-dimensional chains in Ta-intercalated bilayer 2H-TaS_2 with coexisting superconductivity, Phys. Rev. B **107**, L161401 (2023).

[29] E. Morosan, H. W. Zandbergen, B. S. Dennis, J. W. G. Bos, Y. Onose, T. Klimczuk, A. P. Ramirez, N. P. Ong, and R. J. Cava, Superconductivity in Cu_xTiSe_2, Nat. Phys. **2**, 544 (2006).

[30] A. F. Kusmartseva, B. Sipos, H. Berger, L. Forro, and E. Tutis, Pressure induced superconductivity in pristine 1T-$TiSe_2$, Phys. Rev. Lett. **103**, 236401 (2009).

[31] L. J. Li, E. C. T. O'Farrell, K. P. Loh, G. Eda, B. Özyilmaz, and A. H. Castro Neto, Controlling many-body states by the electric-field effect in a two-dimensional material, Nature (London) **529**, 185 (2016).

[32] U. Dutta, P. S. Malavi, S. Sahoo, B. Joseph, and S. Karmakar, Pressure-induced superconductivity in semimetallic 1T-$TiTe_2$ and its persistence upon decompression, Phys. Rev. B **97**, 060503(R) (2018).

[33] S. Xu, P. Yang, K. Chen, Z. Liu, W. Cui, Q. Hu *et al.*, Superconducting phase diagram and the evolution of electronic structure across charge density wave in underdoped 1T-$Cu_\delta TiSe_2$ under hydrostatic pressure, Phys. Rev. B **104**, 134503 (2021).

[34] B. S. Wang, Y. Liu, K. Ishigaki, K. Matsubayashi, J. Cheng, W. Lu, Y. Sun, and Y. Uwatoko, Pressure-induced bulk superconductivity in a layered transition metal dichalcogenide 1T-tantalum selenium, Phys. Rev. B **95**, 220501(R) (2017).

[35] Y. Wu, H. Xing, C.-S. Lian, H. Lian, J. He, W. Duan, J. Liu, Z. Mao, and Y. Liu, Ion intercalation engineering of electronic properties of two-dimensional crystals of 2H-$TaSe_2$, Phys. Rev. Mater. **3**, 104003 (2019).

[36] S. Xu, Z. Liu, P. Yang, K. Chen, J. Sun, J. Dai *et al.*, Superconducting phase diagrams of S-doped 2H-$TaSe_2$ under hydrostatic pressure, Phys. Rev. B **102**, 184511 (2020).

[37] L. Yan, C. Ding, M. Li, R. Tang, W. Chen, B. Liu *et al.*, Modulating charge-density wave order and superconductivity from two alternative stacked monolayers in a bulk 4*Hb*-$TaSe_2$ heterostructure via pressure, Nano Lett. **23**, 2121 (2023).

[38] Y. Qi, P. G. Naumov, M. N. Ali, C. R. Rajamathi, W. Schnelle, O. Barkalov *et al.*, Superconductivity in Weyl semimetal candidate $MoTe_2$, Nat. Commun. **7**, 11038 (2016).

[39] F. C. Chen, X. Luo, R. C. Xiao, W. J. Lu, B. Zhang, H. X. Yang *et al.*, Superconductivity enhancement in the S-doped Weyl semimetal candidate $MoTe_2$, Appl. Phys. Lett. **108**, 162601 (2016).

[40] H. Takahashi, T. Akiba, K. Imura, T. Shiino, K. Deguchi, N. K. Sato, H. Sakai, M. S. Bahramy, and S. Ishiwata, Anticorrelation between polar lattice instability and superconductivity in the Weyl semimetal candidate $MoTe_2$, Phys. Rev. B **95**, 100501(R) (2017).

[41] H. Zhang *et al.*, Enhancement of superconductivity in organic-inorganic hybrid topological materials, Sci. Bull. **65**, 188 (2020).

[42] Y. Zhang, A. Rousuli, S. Shen, K. Zhang, C. Wang, L. Luo *et al.*, Enhanced superconductivity and upper critical field in Ta-doped Weyl semimetal T_d-$MoTe_2$, Adv. Mater. **35**, 2207841 (2023).

[43] E. Revolinsky, G. A. Spiering, and D. J. Beerntsen, Superconductivity in the niobium-selenium system, J. Phys. Chem. Solids **26**, 1029 (1965).

[44] J. J. Hauser, M. Robbins, and F. J. DiSalvo, Effect of 3*d* impurities on the superconducting transition temperature of the layered compound $NbSe_2$, Phys. Rev. B **8**, 1038 (1973).

[45] C. S. Mcewen, D. J. S. Julien, P. P. Edwards, and M. J. Sienko, Structure and superconductivity in lithium-intercalated niobium dichalcogenides, Inorg. Chem. **24**, 1656 (1985).

[46] T. Yokoya, T. Kiss, A. Chainani, S. Shin, M. Nohara, and H. Takagi, Fermi surface sheet-dependent superconductivity in 2H-$NbSe_2$, Science **294**, 2518 (2001).

[47] H. Suderow, V. G. Tissen, J. P. Brison, J. L. Marínez, and S. Vieira, Pressure induced effects on the Fermi surface of superconducting 2H-$NbSe_2$, Phys. Rev. Lett. **95**, 117006 (2005).

[48] I. Naik and A. K. Rastogi, Transport properties of 2H-$NbSe_2$: Effect of Ga-intercalation, Physica B: Condens. Matter **405**, 955 (2010).

[49] M. M. Ugeda, A. J. Bradley, Y. Zhang, S. Onishi, Y. Chen, W. Ruan *et al.*, Characterization of collective ground states in single-layer $NbSe_2$, Nat. Phys. **12**, 92 (2015).

[50] C. S. Lian, C. Si, J. Wu, and W. H. Duan, First-principles study of Na-intercalated bilayer $NbSe_2$: Suppressed charge-density wave and strain-enhanced superconductivity, Phys. Rev. B **96**, 235426 (2017).

[51] H. Wang, X. Huang, J. Lin, J. Cui, Y. Chen, C. Zhu *et al.*, High-quality monolayer superconductor $NbSe_2$ grown by chemical vapour deposition, Nat. Commun. **8**, 394 (2017).

[52] H. Luo, J. Strychalska-Nowak, J. Li, J. Tao, T. Klimczuk, and R. J. Cava, S-shaped suppression of the superconducting transition temperature in Cu-intercalated $NbSe_2$, Chem. Mater. **29**, 3704 (2017).

[53] E. Khestanova *et al.*, Unusual suppression of the superconducting energy gap and critical temperature in atomically thin $NbSe_2$, Nano Lett. **18**, 2623 (2018).

[54] K. Zhao, H. Lin, X. Xiao, W. Huang, W. Yao, M. Yan *et al.*, Disorder-induced multifractal superconductivity in monolayer niobium dichalcogenides, Nat. Phys. **15**, 904 (2019).

[55] X. Fan, H. Chen, L. Zhao, S. Jin, and G. Wang, Quick suppression of superconductivity of $NbSe_2$ by Rb intercalation, Solid State Commun. **297**, 6 (2019).

[56] R. Bianco, L. Monacelli, M. Calandra, F. Mauri, and I. Errea, Weak dimensionality dependence and dominant role of ionic fluctuations in the charge-density-wave transition of $NbSe_2$, Phys. Rev. Lett. **125**, 106101 (2020).

[57] H. Zhang, A. Rousuli, K. Zhang, L. Luo, C. Guo, X. Cong *et al.*, Tailored Ising superconductivity in intercalated bulk $NbSe_2$, Nat. Phys. **18**, 1425 (2022).

[58] S. Naik, S. Kalaiarasan, R. C. Nath, S. N. Sarangi, A. K. Sahu, D. Samal, H. S. Biswal, and S. L. Samal, Nominal effect of Mg intercalation on the superconducting properties of 2H-$NbSe_2$, Inorg. Chem. **60**, 4588 (2021).

[59] S. Naik, A. Pradhan, A. Mishra, and S. L. Samal, Evolution of structural properties in Fe intercalated 2H-$NbSe_2$: Phase transformation induced by strong host-guest interaction, J. Phys. Chem. C **126**, 13762 (2022).

[60] J. T. Ye, Y. J. Zhang, R. Akashi, M. S. Bahramy, R. Arita, and Y. Iwasa, Superconducting dome in a gate-tuned band insulator, Science **338**, 1193 (2012).

[61] J. M. Lu, O. Zheliuk, I. Leermakers, N. F. Yuan, U. Zeitler, K. T. Law, and J. T. Ye, Evidence for two-dimensional Ising superconductivity in gated MoS_2, Science **350**, 1353 (2015).

[62] S. Sahoo, U. Dutta, L. Harnagea, A. K. Sood, and S. Karmakar, Pressure-induced suppression of charge density wave and emergence of superconductivity in 1T-VSe_2, Phys. Rev. B **101**, 014514 (2020).

[63] R. Sereika, C. Park, C. Kenney-Benson, S. Bandaru, N. J. English, Q. Yin, H. Lei, N. Chen, C. J. Sun, S. M. Heald, J. Ren, J. Chang, Y. Ding, and H. K. Mao, Novel superstructure-phase two-dimensional material 1T-VSe_2 at high pressure, J. Phys. Chem. Lett. **11**, 380 (2020).

[64] B. S. de Lima, R. R. de Cassia, F. B. Santos, L. E. Correa, T. W. Grant, A. L. R. Manesco, and A. J. S. Machado, Properties and superconductivity in Ti-doped $NiTe_2$ single crystals, Solid State Commun. **283**, 27 (2018).

[65] Y. Fang, J. Pan, D. Zhang, D. Wang, H. T. Hirose, T. Terashima *et al.*, Discovery of superconductivity in 2M WS_2 with possible topological surface states, Adv. Mater. **31**, 1901942 (2019).

[66] A. Rousuli, H. Zhang, K. Zhang, H. Zhong, R. Feng, Y. Wu, P. Yu, and S. Zhou, Induced anisotropic superconductivity in ionic liquid cation intercalated 1T-$SnSe_2$, 2D Mater. **8**, 015024 (2021).

[67] Y. W. Li, H. J. Zheng, Y. Q. Fang, D. Q. Zhang, Y. J. Chen, C. Chen *et al.*, Observation of topological superconductivity in a stoichiometric transition metal dichalcogenide 2M-WS_2, Nat. Commun. **12**, 2874 (2021).

[68] W. Wang, B. Wang, Z. Gao, G. Tang, W. Lei, X. Zheng, H. Li, X. Ming, and C. Autieri, Charge density wave instability and pressure-induced superconductivity in bulk 1T-NbS_2, Phys. Rev. B **102**, 155115 (2020).

[69] W. Zhang, Y. Fang, Z. Zhang, F. Tian, Y. Huang, X. Wang, X. Huang, F. Huang, and T. Cui, A new superconducting 3R-WS_2 phase at high pressure, J. Phys. Chem. Lett. **12**, 3321 (2021).

[70] J. Guo, C. Huang, H. Luo, H. Yang, L. Wei, S. Cai, Y. Zhou, H. Zhao, X. Li, Y. Li, K. Yang, A. Li, P. Sun, J. Li, Q. Wu, R. J. Cava, and L. Sun, Observation of three superconducting transitions in the pressurized CDW-bearing compound $TaTe_2$, Phys. Rev. Mater. **6**, L051801 (2022).

[71] L. F. Shi, Z. Y. Liu, J. Li, X. X. Zhang, N. N. Wang, Q. Cui *et al.*, Pressure-driven superconducting dome in the vicinity of CDW in the pyrite-type superconductor CuS_2, Phys. Rev. Mater. **6**, 014802 (2022).

[72] F. Wang, Y. Zhang, Z. Wang, H. Zhang, X. Wu, C. Bao, J. Li, P. Yu, and S. Zhou, Ionic liquid gating induced self-intercalation of transition metal chalcogenides, Nat. Commun. **14**, 4945 (2023).

[73] J. G. Si, W. J. Lu, H. Y. Wu, H. Y. Lv, X. Liang, Q. J. Li, and Y. P. Sun, Origin of the multiple charge density wave order in 1T-VSe_2, Phys. Rev. B **101**, 235405 (2020).

[74] Z. Zhang, J. Niu, P. Yang, Y. Gong, Q. Ji, J. Shi *et al.*, Van der Waals epitaxial growth of 2D metallic vanadium diselenide single crystals and their extra-high electrical conductivity, Adv. Mater. **29**, 1702359 (2017).

[75] D. Zhang, J. Ha, H. Baek, Y.-H. Chan, F. D. Natterer, A. F. Myers *et al.*, Strain engineering a $\sqrt{4} \times \sqrt{3a}$ charge-density-wave phase in transition-metal dichalcogenide 1T-VSe_2, Phys. Rev. Mater. **1**, 024005 (2017).

[76] M. Bonilla, S. Kolekar, Y. Ma, H. Coy Diaz, V. Kalappattil, R. Das, T. Eggers, H. R. Gutierrez, M.-H. Phan, and M. Batzill, Strong room-temperature ferromagnetism in VSe_2 monolayers on van der Waals substrates, Nat. Nanotechnol. **13**, 289 (2018).

[77] H. Liu, L. Bao, Z. Zhou, B. Che, R. Zhang, C. Bian *et al.*, Quasi-2D transport and weak antilocalization effect in few-layered VSe_2, Nano Lett. **19**, 4551 (2019).

[78] T. Zhu, D. J. O'Hara, B. A. Noesges, M. Zhu, J. J. Repicky, M. R. Brenner, L. J. Brillson, J. Hwang, J. A. Gupta, and R. K. Kawakami, Coherent growth and characterization of van der Waals 1T-VSe_2 layers on GaAs(111)B using molecular beam epitaxy, Phys. Rev. Mater. **4**, 084002 (2020).

[79] C. J. Sayers, L. S. Farrar, S. J. Bending, M. Cattelan, A. J. H. Jones, N. A. Fox, G. Kociok-Köhn, K. Koshmak, J. Laverock, L. Pasquali, and E. Da Como, Correlation between crystal purity and the charge density wave in 1T−VSe_2, Phys. Rev. Mater. **4**, 025002 (2020).

[80] P. Chen, W. W. Pai, Y. H. Chan, V. Madhavan, M. Y. Chou, S. K. Mo, A. V. Fedorov, and T. C. Chiang, Unique gap structure and symmetry of the charge density wave in single-layer VSe_2, Phys. Rev. Lett. **121**, 196402 (2018).

[81] J. Feng, D. Biswas, A. Rajan, M. D. Watson, F. Mazzola, O. J. Clark *et al.*, Electronic structure and enhanced charge-density wave order of monolayer VSe_2, Nano Lett. **18**, 4493 (2018).

[82] G. Duvjir, B. K. Choi, I. Jang, S. Ulstrup, S. Kang, T. T. Ly *et al.*, Emergence of a metal-insulator transition and high-temperature charge-density waves in VSe_2 at the monolayer limit, Nano Lett. **18**, 5432 (2018).

[83] A. O. Fumege, M. Gobbi, P. Dreher, W. Wan, C. González-Orellana, M. Peña-Díaz *et al.*, Absence of ferromagnetism in VSe_2 caused by its charge density wave phase, J. Phys. Chem. C **123**, 27802 (2019).

[84] W. Jolie, T. Knispel, N. Ehlen, K. Nikonov, C. Busse, A. Grüneis, and T. Michely, Charge density wave phase of VSe_2 revisited, Phys. Rev. B **99**, 115417 (2019).

[85] Y. Falke, N. Ehlen, G. Marini, A. V. Fedorov, V. Y. Voroshnin, B. V. Senkovskiy *et al.*, Coupling to zone-center optical phonons in VSe_2 enhanced by charge density waves, Phys. Rev. B **104**, 235137 (2021).

[86] G. Duvjir, B. Choi, T. T. Ly, N. H. Lam, K. Jang, D. D. Dung, Y. Chang, and J. Kim, Multiple charge density wave phases of monolayer VSe_2 manifested by graphene substrates, Nanotechnology **32**, 364002 (2021).

[87] L. Yin, T. Berlijn, R. Juneja, L. Lindsay, and D. S. Parker, Competing magnetic and nonmagnetic states in monolayer VSe_2 with charge density wave, Phys. Rev. B **106**, 085117 (2022).

[88] A. H. Thompson and B. G. Silbernagel, Correlated magnetic and transport properties in the charge-density-wave states of VSe_2, Phys. Rev. B **19**, 3420 (1979).

[89] K. Tsutsumi, X-ray-diffraction study of the periodic lattice distortion associated with a charge-density wave in 1T-VSe_2, Phys. Rev. B **26**, 5756 (1982).

[90] D. J. Eaglesham, R. L. Withers, and D. M. Bird, Charge-density-wave transitions in 1T-VSe_2, J. Phys. C **19**, 359 (1986).

[91] K. Terashima, T. Sato, H. Komatsu, T. Takahashi, N. Maeda, and K. Hayashi, Charge-density wave transition of 1T-VSe_2 studied by angle-resolved photoemission spectroscopy, Phys. Rev. B **68**, 155108 (2003).

[92] G. Chen, S. T. Howard, A. B. Maghirang, III, K. Nguyen Cong, R. Angelo B. Villaos, L.-Y. Feng, K. Cai, S. C. Ganguli, W. Swiech, E. Morosan, I. I. Oleynik, F.-C. Chuang, H. Lin, and V. Madhavan, Correlating structural, electronic, and magnetic properties of epitaxial VSe_2 thin films, Phys. Rev. B **102**, 115149 (2020).

[93] J. Diego, A. H. Said, S. K. Mahatha, R. Bianco, L. Monacelli, M. Calandra, F. Mauri, K. Rossnagel, I. Errea, and S. B. Canosa, van der Waals driven anharmonic melting of the 3D charge density wave in VSe_2, Nat. Commun. **12**, 598 (2021).

[94] T. Yilmaz and E. Vescovo, Revealing flat bands near the Fermi level in 1T-VSe_2 by using angle-resolved photoemission spectroscopy, Phys. Rev. B **105**, L041101 (2022).

[95] Z. Guo, X. Hao, J. Dong, H. Li, J. Liao, and D. Chen, Observation of pressure induced charge density wave order and eightfold structure in bulk VSe_2, Sci. Rep. **11**, 18157 (2021).

[96] P. Giannozzi, S. Baroni, N. Bonini, M. Calandra, R. Car, C. Cavazzoni *et al.*, QUANTUM ESPRESSO: A modular and open-source software project for quantum simulations of materials, J. Phys.: Condens. Matter **21**, 395502 (2009).

[97] P. Giannozzi, O. Andreussi, T. Brumme, O. Bunau, M. B. Nardelli, M. Calandra *et al.*, Advanced capabilities for materials modelling with Quantum ESPRESSO, J. Phys.: Condens. Matter **29**, 465901 (2017).

[98] G. Kresse and D. Joubert, From ultrasoft pseudopotentials to the projector augmented-wave method, Phys. Rev. B **59**, 1758 (1999).

[99] J. P. Perdew, K. Burke, and M. Ernzerhof, Generalized Gra dient approximation made simple, Phys. Rev. Lett. **77**, 3865 (1996).

[100] D. M. Ceperley and B. J. Alder, Ground state of the electron gas by a stochastic method, Phys. Rev. Lett. **45**, 566 (1980).

[101] M. Kawamura, FermiSurfer: Fermi-surface viewer providing multiple representation schemes, Comput. Phys. Commun. **239**, 197 (2019).

[102] F. Giustino, Electron-phonon interactions from first principles, Rev. Mod. Phys. **89**, 015003 (2017).

[103] G. M. Eliashberg, Interactions between electrons and lattice vibrations in a superconductor, Sov. Phys. JETP **11**, 696 (1960) [J. Exptl. Theoret. Phys. (U.S.S.R.) **38**, 1438 (1960)].

[104] P. B. Allen and R. C. Dynes, Transition temperature of strong coupled superconductors reanalyzed, Phys. Rev. B **12**, 905 (1975).

[105] M. Bayard and M. J. Sienko, Anomalous electrical and magnetic properties of vanadium diselenide, J. Solid State Chem. **19**, 325 (1976).

[106] M. Lazzeri and F. mauri, Nonadiabatic kohn anomaly in a doped graphene monolayer, Phys. Rev. Lett. **97**, 266407 (2006).

[107] W. Yang, Y. Yang, F. W. Zheng, and P. Zhang, Vibration responses of *h*-BN sheet to charge doping and external strain, J. Chem. Phys. **139**, 214708 (2013).

[108] Z.-G. Fu, Z.-Y. Hu, Y. Yang, Y. Lu, F.-W. Zheng, and P. Zhang, Modulation of doping and biaxial strain on the transition temperature of the charge density wave transition in 1T-$TiSe_2$, RSC Adv. **6**, 76972 (2016).

[109] G. Pizzi, V. Vitale, R. Arita, S. Blügel, F. Freimuth, G. Géranton *et al.*, Wannier90 as a community code: New features and applications, J. Phys.: Condens. Matter **32**, 165902 (2020).

[110] X. Wang, X. Chen, Y. Zhou, C. Park, C. An, Y. Zhou, R. Zhang, C. Gu, W. Yang, and Z. Yang, Pressure-induced isostructural phase transition and metallization in WSe_2, Sci. Rep. **7**, 46694 (2017).

[111] V. Rajaji, U. Dutta, P. C. Sreeparvathy, S. C. Sarma, Y. A. Sorb, B. Joseph, S. Sahoo, S. C. Peter, V. Kanchana, and C. Narayana, Structural, vibrational, and electrical properties of 1T-$TiTe_2$ under hydrostatic pressure: Experiments and theory, Phys. Rev. B **97**, 085107 (2018).

[112] A. P. Roy, N. Bajaj, R. Mittal, P. D. Babu, and D. Bansal, Quasi one-dimensional fermi surface nesting and hidden nesting enable multiple Kohn anomalies in α-uranium, Phys. Rev. Lett. **126**, 096401 (2021).

[113] P.-F. Liu, F. Zheng, J. Li, J.-G. Si, L. Wei, J. Zhang, and B.-T. Wang, Two-gap superconductivity in a Janus MoSH monolayer, Phys. Rev. B **105**, 245420 (2022).

[114] Z. H. Huo, D. F. Duan, T. C. Ma, Z. H. Zhang, Q. W. Jiang, D. C. An, H. Song, F. B. Tian, and T. Cui, First-principles study on the conventional superconductivity of N-doped fcc-LuH3, Matter Radiat. Extremes **8**, 038402 (2023).

[115] A. Yang, X. Tao, Y. Quan, and P. Zhang, First-principles investigation of the origin of superconductivity in $TlBi_2$, Phys. Rev. B **108**, 075203 (2023).

[116] T. T. Pham and D. L. Nguyen, First-principles prediction of superconductivity in MgB_3C_3, Phys. Rev. B **107**, 134502 (2023).

[117] W. Sun, B. Chen, X. Li, F. Peng, A. Hermann, and C. Lu, Ternary NaPH superconductor under high pressure, Phys. Rev. B **107**, 214511 (2023).

[118] Z. W. Liao, X. W. Yi, J. Y. You, B. Gu, and G. Su, Family of binary transition metal pnictide superconductors, Phys. Rev. B **108**, 014501 (2023).

[119] X. Yuan, Y. Zhang, J. Hao, M. Xu, and Y. Li, Pressure-induced ternary Li-Mn-B compounds: A first-principles study, Phys. Rev. Res. **5**, 043114 (2023).

[120] W. Sukmas, P. Tsuppayakorn-aek, P. Pluengphon, S. J. Clark, R. Ahuja, T. Bovornratanaraks, and W. Luo, First-principles calculations on superconductivity and H-diffusion kinetics in Mg-B-H phases under pressures, Inter. J. Hydrogen Energy **48**, 4006 (2023).

[121] B. T. Wang, P. F. Liu, J. J. Zheng, W. Yin, and F. Wang, First-principles study of superconductivity in the two-and three-dimensional forms of $PbTiSe_2$: Suppressed charge density wave in 1T-$TiSe_2$, Phys. Rev. B **98**, 014514 (2018).

[122] T. J. Kim, S. Ryee, M. J. Han, and S. Choi, Dynamical mean-field study of vanadium diselenide monolayer ferromagnetism, 2D Mater. **7**, 035023 (2020).

[123] C. Zhang, J. Sous, D. R. Reichman, M. Berciu, A. J. Millis, N. V. Prokof'ev, and B. V. Svistunov, Bipolaronic high-temperature superconductivity, Phys. Rev. X **13**, 011010 (2023).